Available online at www.sciencedirect.com

ScienceDirect

Geochimica et Cosmochimica Acta 217 (2017) 421–440

Geochimica et Cosmochimica Acta

www.elsevier.com/locate/gca

A reactive transport model for Marcellus shale weathering

Peyman Heidari [a,1], Li Li [b,*], Lixin Jin [c], Jennifer Z. Williams [d], Susan L. Brantley [d,e]

[a] John and Willie Leone Family Department of Energy and Mineral Engineering, Pennsylvania State University, University Park, PA, United States

[b] Department of Civil & Environmental Engineering, Pennsylvania State University, University Park, PA, United States

[c] Department of Geological Sciences, University of Texas at El Paso, El Paso, TX, United States

[d] Department of Geosciences, Pennsylvania State University, University Park, PA, United States

[e] Earth and Environmental Systems Institute, Pennsylvania State University, University Park, PA, United States

Received 29 August 2016; accepted in revised form 3 August 2017; available online 8 August 2017

Abstract

Shale formations account for 25% of the land surface globally and contribute a large proportion of the natural gas used in the United States. One of the most productive shale-gas formations is the Marcellus, a black shale that is rich in organic matter and pyrite. As a first step toward understanding how Marcellus shale interacts with water in the surface or deep subsurface, we developed a reactive transport model to simulate shale weathering under ambient temperature and pressure conditions, constrained by soil and water chemistry data. The simulation was carried out for 10,000 years since deglaciation, assuming bedrock weathering and soil genesis began after the last glacial maximum. Results indicate weathering was initiated by pyrite dissolution for the first 1000 years, leading to low pH and enhanced dissolution of chlorite and precipitation of iron hydroxides. After pyrite depletion, chlorite dissolved slowly, primarily facilitated by the presence of CO_2 and organic acids, forming vermiculite as a secondary mineral.

A sensitivity analysis indicated that the most important controls on weathering include the presence of reactive gases (CO_2 and O_2), specific surface area, and flow velocity of infiltrating meteoric water. The soil chemistry and mineralogy data could not be reproduced without including the reactive gases. For example, pyrite remained in the soil even after 10,000 years if O_2 was not continuously present in the soil column; likewise, chlorite remained abundant and porosity remained small if CO_2 was not present in the soil gas. The field observations were only simulated successfully when the modeled specific surface areas of the reactive minerals were 1–3 orders of magnitude smaller than surface area values measured for powdered minerals. Small surface areas could be consistent with the lack of accessibility of some fluids to mineral surfaces due to surface coatings. In addition, some mineral surface is likely interacting only with equilibrated pore fluids. An increase in the water infiltration rate enhanced weathering by removing dissolution products and maintaining far-from-equilibrium conditions. We conclude from these observations that availability of reactive surface area and transport of H_2O and gases are the most important factors affecting rates of Marcellus shale weathering of the in the shallow subsurface. This weathering study documents the utility of reactive transport modeling for complex subsurface processes. Such modelling could be extended to understand interactions between injected fluids and Marcellus shale gas reservoirs at higher temperature, pressure, and salinity conditions.

Keywords: Chemical weathering; Reactive transport modeling; Critical zone; Marcellus shale

* Corresponding author.
E-mail address: lili@engr.psu.edu (L. Li).

[1] Current address: Department of Geosciences and Geological and Petroleum Engineering, Missouri University of Science and Technology, Rolla, MO, United States.

http://dx.doi.org/10.1016/j.gca.2017.08.011
0016-7037/

1. INTRODUCTION

Exposed shale formations account for 25% of the land surface globally (Suchet et al., 2003). Subsurface shales are now contributing close to half of the natural gas used in the United States. Of particular importance in gas production are black shale formations that are rich in organic material – and which also host high concentrations of trace and heavy metals (Jaffe et al., 2002; Tuttle and Breit, 2009). To extract gas, high-volume hydraulic fracturing is used to open the rocks and expose them to large volumes of water. Various environmental issues can arise as a result of shale gas development related to the return of metal- and organic-containing high salinity water to the land surface (Vidic et al., 2013; Warner et al., 2013; Brantley et al., 2014). Trace metals are also released during weathering of black shale at the land surface (Liermann et al., 2011; Chapman et al., 2012; Phan et al., 2015; Stewart et al., 2015). While very few data are available to constrain water-rock interaction at high temperature in the deep subsurface (Balashov et al., 2015), observations from chemical weathering in the shallow subsurface are more readily available (Jin et al., 2013). Here we investigate water-rock interaction in the Marcellus shale by focusing on surficial processes where we have observational data to constrain model simulations. Such models can be used to understand dominant water-rock interaction processes, identify major controls of soil formation and soil water chemistry, and quantify kinetics of mineral dissolution and thus release rates of rock-forming elements. The model provides a stepping stone toward the prediction of water-rock interactions at higher temperature, pressure, and salinity during hydraulic fracturing. In addition, such models can be used to understand black shale weathering, the long-term controls on oxygen over geologic time, and acid mine / rock drainage.

Mineral weathering and soil formation have previously been observed to depend on the infiltration of meteoric waters (Brantley and White, 2009), the rate of erosion (Millot et al., 2002; Riebe et al., 2004; West et al., 2005), and the composition of reacting fluids (Oelkers et al., 1994). The nature and concentration of acids in pore waters also control weathering. For example, biological activity often results in the production of organic acids that can change mineral dissolution rates by lowering pH, accelerating the rates toward equilibration (Drever and Stillings, 1997), and enhancing aqueous complexation (Lawrence et al., 2014). Likewise, soil pCO_2 also controls weathering rates of granitic parent material (Moore et al., 2012). Weathering of gray shale of the Rose Hill formation was observed to initiate via pyrite oxidative dissolution at 23 m depth under a ridge, followed by the dissolution of illite and chlorite that formed vermiculite and iron oxide-hydroxides at shallower depths in the organic poor soil (0.03–0.05 wt%) (Jin et al., 2010, 2013, 2014; Liermann et al., 2011). These processes increased permeability and water accessibility, and exposed other minerals to weathering (Brantley et al., 2013).

In the past decades, reactive transport models (RTMs) have advanced significantly and have been used widely to understand, quantify, and predict chemical weathering, geological carbon sequestration and other processes (Hausrath et al., 2008; Li et al., 2017b; Lichtner, 1992; Steefel et al., 2005; Zheng et al., 2009). In general, simulation of chemical weathering has focused on one-dimensional analysis. The RTM studies have found that rates and extent of weathering are controlled by intrinsic variables such as mineralogy, protolith porosity, surface area, as well as extrinsic variables such as climate. Hausrath et al. (2008) showed that dominant reactions during basalt weathering include the dissolution of feldspars and augite and precipitation of kaolinite and iron oxide-hydroxides. Navarre-Sitchler et al. (2011) analyzed basalt weathering rinds and found that plagioclase and augite dissolved while gibbsite, kaolinite, and goethite precipitated, leading to drastic increase in pore connectivity and diffusion in bedrock. Bolton et al. (2006) recently modelled weathering of the New Albany black shale to understand geologic controls on oxygen in the atmosphere. Other field and laboratory-oriented studies also explored the shale weathering and metal release (Jaffe et al., 2002; Tuttle and Breit, 2009; Tuttle et al., 2009). Our understanding on weathering of Marcellus shale, however, is rather limited.

Given the importance of understanding water-shale interactions at depth (for shale gas) and near the surface (for metal contamination of water resources), we developed a reactive transport model for Marcellus shale weathering as a first step toward quantitative understanding and prediction of water-shale interactions over a full range of temperature and pressure conditions. Importantly, water chemistry data can constrain the rates of processes at decadal timescales (i.e. the residence time of meteoric waters in soil profiles) and soil chemistry data can constrain the rates of weathering processes over millennia (i.e., the residence time of solid materials in soil profiles (Brantley, 2010). RTMs can then be used to integrate across these time scales, as well as to history match and forecast various weathering stages under changing conditions.

2. METHODOLOGY

2.1. The Marcellus shale

This study focuses on weathering of black shale of the Oatka Creek member of the Middle Devonian Marcellus Formation within the Hamilton group. The Marcellus formation underlies much of Pennsylvania, extending into Ohio, West Virginia, and New York (Obermajer et al., 1997). The Marcellus Formation at kilometers depth has been the target of extensive drilling and high-volume hydraulic fracturing since 2004 (Brantley et al., 2014); however here we focus on weathering of outcrops. Samples of bedrock, soil and soil water were collected from a forested northwest-facing planar hillslope, located in Jackson Corner, Huntingdon County, Pennsylvania.

2.2. Soil and water sampling and analysis

The field site and sample collection have been previously described (Mathur et al., 2012; Jin et al., 2013) and are

briefly introduced below. Soil profiles were sampled using a hand auger along a roughly planar but convex-upward hillslope on Marcellus shale. The hillslope is defined between two general sampling locations sited within 10 m of one another: the first at the ridge top (augered cores at sites RT1 and RT2) and the second at a valley floor location (VFS) at an elevation 30 m below the ridgetop. The entire slope is developed.

Bulk elemental chemistry was measured on the RT and VFS samples (i.e., without removal of any particle size fraction). Here we present elemental chemistry of soil pore water sampled from three nests of lysimeters (soil water samplers: http://www.soilmoisture.com/1900L-Near-Surface-Samplers/) installed May 2010 at the ridgetop (labelled as the MRT site), middle slope (MMS), and valley floor (MVF) along the same Marcellus transect (see Fig. 1 in Mathur et al. (2012)). The diameter of the lysimeters is 4.8 cm. The ceramic frit at the bottom allows water to enter and extend for 5 cm in the long dimension of the tube. The vacuum is always set up at 0.5 cbar, so the lateral average that contributes water to the lysimeters varies depending on the soil moisture content. At each of the three locations, several lysimeters were emplaced at ~10 cm depth intervals (see Table B1 for depths at each location). Before emplacement, lysimeters (from Soil Moisture Equipment Corp 1900 series) were washed with 10% nitric acid and rinsed repeatedly with double deionized water. Samples collected at MRT, MMS, and MVF during lysimeter emplacement were also analyzed for bulk density.

Soil pore waters were collected at roughly weekly intervals starting two weeks after lysimeter emplacement. A hand pump was used to pull vacuum on the lysimeters to −50 centibars one week before each collection. Water sampling was carried out by lowering PVC tubing into the ceramic cup and pumping water out with a syringe. The pH was measured with a pH meter and an electrode (SymPhony

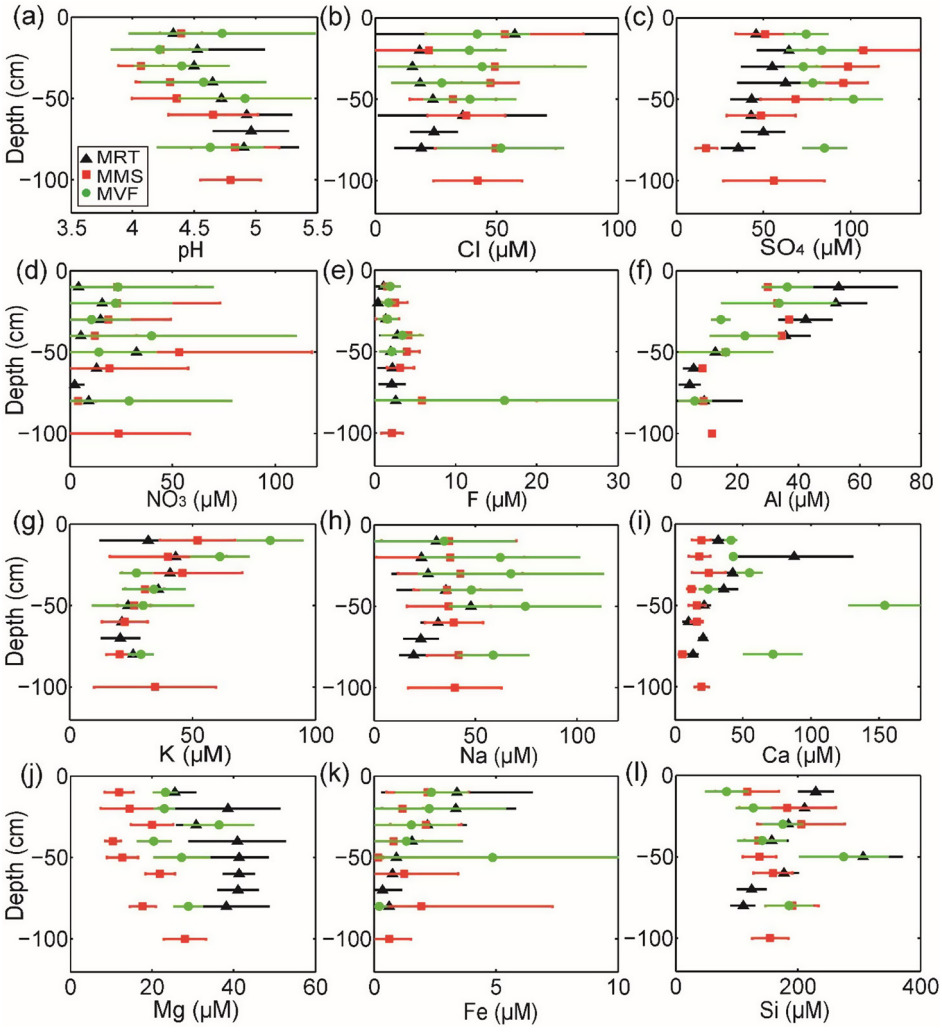

Fig. 1. Water chemistry data versus depth at different sampling locations: ridge top (MRT), mid slope (MMS), and valley floor (MVF). Symbols represent the average values at each location and depth as measured in approximately 240 samples taken between 05/14/2010 and 12/02/11 (all values included in Table B1 in Supplementary Information). Mean and standard deviation values are reported in Tables B2 and B3. Values of pH increase with depth. Silica was present at the highest concentration. Sulfate and chloride were the dominant anions. Al, Fe, and K consistently decreased with depth at all three locations. Na and Mg concentrations remained relatively constant as a function of depth.

SP70P) calibrated with standard pH buffers (4 and 7). Aliquots (30 mL) were then acidified with 5 drops of ultrapure nitric acid and stored in pre-cleaned high density polyethylene (HDPE) bottles for cation analysis. Acidified pore water samples were analyzed for major cation concentrations using inductively coupled plasma atomic emission spectrometry (ICP-AES) (Perkin-Elmer Optima 5300). A similar aliquot was stored without acid addition for anion analysis using a Dionex ion chromatograph (ICS-2500).

2.3. Bedrock and soil samples

Jin et al. (2013) and Mathur et al. (2012) investigated a total of 8 rock samples that were assumed to give an indication of parent composition: 4 derived from a nearby road outcrop sampled at 5 m depth below the land surface, and 4 from the bottom of the augered soil cores. The organic carbon content of the putative parent rocks varied, as expected given that the Marcellus formation (including the Oatka creek member sampled here) has highly variable organic content throughout Pennsylvania. Four of the 8 parent samples were observed to contain organic carbon (1.16–1.39 wt.% C) on average lower than those observed in deep core samples of the most common production target for shale gas in Pennsylvania, the Union Springsmember of the Marcellus formation (1.9–7.3 wt.%) (Gu et al., 2015). The parent samples for the Marcellus in this study were much lower in C than those observed at depth between 9 and 13 m in the New Albany black shale, 8–16 wt% C (Wildman et al., 2004).

The deep-core samples were also observed to contain 0.29–1.53 wt% S. These values are much larger than the S content (0.023 wt%) in a sample analyzed from the bottom of the RT1 core from the top 2.5 m. Thus, it was inferred that pyrite had begun oxidatively dissolving from the parent material at tens of meter depth (Jin et al., 2013). Very little S was retained in the <2 mm fraction of soil; however, rock chips in the soil were observed to occasionally contain pyrite under electron microscopy. This deep depletion of pyrite is similar to observations for the New Albany black shale where about 6.9 wt% S was observed at 8 m depth while only 0.3–0.5 wt% of S was observed within the top 2.5 m (Wildman et al., 2004). We therefore cannot use relatively shallow samples to determine parent carbon content because it is likely that organic carbon is depleted from the shale at tens of meters of depth, i.e., deeper than the samples in this study (Jin et al., 2013). Deep oxidative dissolution of pyrite in the Marcellus is attributed to deep penetration of O_2-containing water. Such penetration is expected given the likelihood of deep fracturing during the periglacial period associated with the Last Glacial Maximum.

Based on X-ray diffraction analyses of bedrock samples, the dominant minerals in the Marcellus shale are chlorite, illite, vermiculite, iron oxide-hydroxide, quartz and pyrite (Mathur et al., 2012; Jin et al., 2013). For two soil samples from RT1 core (from 20 to 26 cm depth and from 109 to 115 cm depth), clays were treated to separate minerals following the methods of Poppe et al. (2002). This included ethylene glycol treatment, K saturation treatment, Mg saturation treatment, and acid treatment. The clay-sized minerals were identified to be chlorite (14, 7.2 and 3.5 Å peaks), illite (10, 5 and 3.3 Å peaks), vermiculite (14 Å peak), a small amount of quartz (4.3 and 3.3 Å peaks) and possibly kaolinite with a small particle size (broad 7.2 and 3.6 Å peaks). The occurrence of kaolinite cannot be conclusively determined due to the presence of chlorite and its very low abundance (if it is present at all).

2.4. Rain water chemistry

Annual rainfall averages 1.0 m in this study area (Jin et al., 2011). Two National Atmospheric Deposition Program sites in central Pennsylvania (PA-15 and PA-42) show very similar rainwater chemistry. The rainfall concentrations used as model inputs were therefore determined from the monthly averages from both sites during 2006–2008 (Table A1 in Supplementary Information). Due to the acid rain in this part of Pennsylvania, the dominant anions today are SO_4^{2-} and NO_3^-. Dominant cations are Ca^{2+}, Na^+, and H^+, followed by $Mg^{2+}$and K^+. Our study modeled chemical weathering for 10,000 years. However, acid rain deposition was only important for the last 100 years due to increases in S and N emissions related to hydrocarbon burning. Therefore, we set the rainfall chemistry for the first 9900 years at pH 5.5. For the last 100 years, the dissolved CO_2 concentration in rain was increased to set a pH at 4.4, a value within the typical acid rain pH range of 4.2–4.4. Ions in pore water can become concentrated due to evapotranspiration (ET). In central Pennsylvania, ET is reported to be approximately half of the atmospheric precipitation (Jin et al., 2011). To account for this, we followed the approach of other researchers (e.g. Moore et al., 2012) and multiplied the average rainwater ion concentrations by 2.0 to approximate the effect of evapotranspiration during infiltration.

2.5. Reactive transport modeling

The code CrunchFlow was used to simulate the reaction and transport processes. The operator-splitting scheme was implemented in the code using the Strang scheme, in which a half transport step is followed by a full reaction step which is in turn followed by another half transport step (Strang, 1968; Zysset et al., 1994). Reactions in natural systems include both kinetically-controlled reactions and fast, thermodynamically-controlled reactions. Concentrations of species involved in fast reactions such as aqueous complexation are related through the laws of mass action (equilibrium constants). CrunchFlow divides the species into primary and secondary species. The secondary species are written in terms of the primary species using the equilibrium constants of fast reactions. Therefore, the number of equations that the code solves reduces to the number of the primary species instead of the total number of species, which reduces the computation expenses. The list of primary and secondary species is in Table A2 in Supplementary Information.

CrunchFlow solves mass conservation equations and has been used extensively (Steefel et al., 2015). CrunchFlow

solves advection-dispersion-reaction equations for the primary species i:

$$\frac{\partial(\phi C_i)}{\partial t} = \frac{\partial^2(DC_i)}{\partial^2 x} - \frac{\partial(uC_i)}{\partial x} + \sum_{j=1}^{nr} R_{i,j}, \quad i = 1, \ldots, np \qquad (1)$$

where x increases in the downward direction, C_i is the solute concentration of species i (mol/m^3), np is the total number of primary species, u is Darcy flow velocity (m^3/m^2/s), t is time (s), and D is the dispersion coefficient (m^2/s). This latter coefficient is a combination of diffusion and dispersion calculated by the following:

$$D = D^* + \alpha \cdot u \qquad (2)$$

where D^* is the effective diffusion coefficient in porous media (m^2/s) and α is the dispersivity (m). In this work, α was set to 0.0005 m, a value calculated for homogenous sand columns (Salehikhoo et al., 2013). The D^* is calculated as $\phi^m D_0$, where D_0 is the aqueous diffusion coefficient (1.0×10^{-9} m^2/s) and m is the cementation factor with a value of 2.0 (Armatas, 2006). The reaction network also includes mineral dissolution and precipitation that are kinetically-controlled as well as aqueous complexation that is thermodynamically controlled. The classical Transition-State-Theory (TST) based rate laws were used to represent the kinetics of mineral reaction j (Lasaga, 1998):

$$R_{i,j} = A_j\left(k_{j,\mathrm{H}^+} a_{\mathrm{H}}^{n_{\mathrm{H}}} + k_{j,\mathrm{H_2O}} + k_{j,\mathrm{OH}} a_{\mathrm{OH}}^{n_{\mathrm{OH}}}\right)\left(1 - \frac{IAP_j}{K_{eq,j}}\right) \qquad (3)$$

Here $R_{i,j}$ is the reaction rate of mineral j that the species i is involved (mol/m^3/s), A_j is the surface area of a given mineral j per unit volume (which is dependent on mineral abundance (m^2/m^3)), k_j ($k_{j,\mathrm{H}}, k_{j,\mathrm{H_2O}}, k_{j,\mathrm{OH}}$) are the rate constants of mineral j under acidic, neutral, and alkaline conditions (mol m^{-2} s^{-1}); the activities (a) are for H^+, water, and OH^-, IAP_j is the ion activity product, and $K_{eq,j}$ is the equilibrium constant of the mineral reaction j. The saturation index IAP$_j$/$K_{eq,j}$ quantifies how far the aqueous phase is from equilibrium. At equilibrium, IAP$_j$/$K_{eq,j}$ equals 1.0. When the saturation index is less than one, the mineral dissolves and $R_{i,j}$ is positive. When the saturation index is more than one, the solution is oversaturated and precipitation occurs. The term $\Sigma R_{i,j}$ in Eq. (1) is the summation over all relevant removal and addition of aqueous species i by dissolution and precipitation of mineral j that are controlled by kinetics.

All simulations were carried out at 25 °C using the thermodynamic and kinetic parameters in Table 1, which is based on detailed characterization and quantification of mineralogy on the Marcellus Shale parent rock. Combined heat and chemical treatments with XRD revealed that no smectite was present. In the nearby Shale Hills Critical Zone Observatory where we have investigated soils on the Rose Hills (gray) shale, we observed that chlorite and illite react to vermiculite and HIV and a small amount of kaolinite. In that system, the starting clay mineralogy was the same (chlorite, illite, no smectite), although with different proportions. We therefore modelled the weathering of the Marcellus by making defensible and simplified assumptions. First, although amorphous Fe oxides or oxyhydroxides may form as intermediate phases, given the longer timescale of this RTM simulate, we assumed goethite was the most stable phase. Goethite is really a representative iron oxide in the model – it represents the average behavior of iron oxides in the model. Likewise, although we know that HIV may be forming, we chose vermiculite as the stable phase that retains Mg in the soil. At Shale Hills we observed no evidence for precipitation of illite. In the model illite reaction can occur in both dissolution and precipitation directions however we do not observe illite precipitation in the model either. To simulate goethite and vermiculite as the secondary phases, we set their initial volume fractions close to zero to provide "seeds" for precipitation to occur in the model. We used initial specific surface areas from the literature value, because the precipitation "seeds" are assumed to be small and are similar to SSA of mineral powders measured using BET method. The SSA of the precipitating minerals however are not to be interpreted as representing laboratory-field rate differences. In summary, our choice for inclusion of minerals in the RTM is somewhat of a balance chosen among the constraints of the full complexity of what is in the soil, the limitations of the RTM, and the choice of kinetic data from the literature.

A 1D reactive transport model was set up with the assumption that the flow is primarily in the vertical direction. This is particularly the case at the ridge top. The water chemistry and soil profile data at the ridgetop therefore were used to constrain the model. The code simulates single-phase saturated flow without gas phases. In this way we are not simulating the details of multiphase flow in unsaturated zones however represent the average water-rock contact that drives chemical weathering at the geological time scale. Indeed, many RTMs are used to simulate weathering without including an explicit gas phase (Lebedeva et al., 2007). The annual net precipitation (precipitation – evapotranspiration) in central Pennsylvania, approximately 0.50 m/year, was used as the first try for average flow velocity. Under such flow conditions, the Peclet number is around 20, meaning that diffusion and dispersion processes are relatively slow compared to the advection process. At Mid slope and Valley floor sites, lateral flow becomes important and hydrological conditions are more complex so that the systems cannot be modeled as 1D columns. The soil column was assumed to be 120 cm thick, as observed in the ridge top. The simulation domain included a total of 1200 grid blocks. The optimum grid size (0.1 cm × 0.1 cm) was chosen by increasing the resolution until the effluent concentrations did not change with further increases. The top boundary has a constant concentration condition such that incoming porewater chemistry equals the water chemistry that doubles the concentrations of species in the rainwater. This "doubling" was to take into account of evapotranspiration processes that takes about half of the total rainfall at the field site (Jin et al., 2013). The bottom has fixed concentration boundary, meaning the concentrations in the last grid block are the same as the concentrations coming out of the domain.

Table 1
Minerals, reactions, and thermodynamic and kinetic parameters.[a]

Minerals	Initial Volume fraction	Reaction	Log (K_{eq})	Mineral dissolution rate law (mol/m^2/s)	SSA used in this model (m^2/g)	SSA in literature (m^2/g)
Quartz	0.400	$SiO_2 \leftrightarrow SiO_{2(aq)}$	−4.000	[i] $10^{-11.5}\ a_{H+}^{0.35} + 10^{-13.39} + 10^{-10.5}\ a_{OH-}^{0.5}$	1.0×10^{-3}	[b] 1.0×10^{-3}–2.3×10^{0}
Illite	0.200	$Mg_{0.18}Fe_{0.4}K_{0.7}Al_{3.4}Si_{1.0}H_{7.94}O_{12.0} + 12.06\ H^+ \leftrightarrow 0.18\ Mg^{2+} + 0.4\ Fe^{2+} + 0.7K^+ + 3.4\ Al^{3+} + 1.0\ SiO_{2(aq)} + 10\ H_2O$	9.026	[j] $10^{-11.80}\ a_{H+}^{0.51} + 10^{-12.48}\ a_{OH-}^{0.28}$	6.5×10^{0}	[c] 4.2×10^{1}–1.37×10^{2}
Pyrite	0.020	$FeS_2 + H_2O + 3.5\ O_2 \leftrightarrow 2\ H^+ + 2\ SO_4^{2-} + Fe^{2+}$	107.670	[k] $10^{-8.19}\ a_{H+}^{-0.11}\ a_{O2}^{0.5}$	2.0×10^{-3}	[d] 5.0×10^{-2}–2.3×10^{0}
Albite	0.018	$NaAlSi_3O_8 + 4H^+ \leftrightarrow Na^+ + Al^{3+} + 3\ SiO_{2(aq)} + 2\ H_2O$	2.760	[l] $10^{-9.5}\ a_{H+}^{0.5} + 10^{-12.6} + 10^{-9.95}\ a_{OH-}^{0.3}$	5.0×10^{-3}	[e] 4.2×10^{-2}–4.9×10^{-1}
Chlorite	0.300	$Mg_{1.04}Fe_{0.2}K_{1.28}\ Al_{2.24}Si_3H_{13.52}O_{18} + 10.48H^+ \leftrightarrow 1.04\ Mg^{2+} + 0.2\ Fe^{2+} + 1.28K^+ + 2.24Al^{3+} + 3\ SiO_{2(aq)} + 12\ H_2O$	14.996	[m] $10^{-10.77}\ a_{H+}^{0.26} + 10^{-10.99}\ a_{OH-}^{0.39}$	8.0×10^{-1}	[f] 1.1×10^{0}–7.7×10^{0}
Vermiculite	0.000	$Mg_{0.2}Fe_{0.4}K_{1.3}\ Al_{4.4}Si_{1.6}H_{8.5}O_{15.2} + 15.5H^+ \leftrightarrow 0.2\ Mg^{2+} + 0.4\ Fe^{2+} + 1.3K^+ + 4.4\ Al^{3+} + 1.6\ SiO_{2(aq)} + 12\ H_2O$	−5.390	[n] $10^{-11.38}\ a_{H+}^{0.33}$	9.0×10^{-1}	[g] 7.3×10^{-1}–1.74×10^{1}
Goethite	0.000	$Fe(OH)_3 + 2H^+ \leftrightarrow 0.25\ O_{2(aq)} + Fe^{2+} + 2.5\ H_2O$	−7.334	$10^{-8.4}$	3.0×10^{1}	[h] 4.7×10^{1}–2.59×10^{2}
Porosity	0.06					

[a] Although average annual temperature is about 15 °C, rate constants at 25 °C are used to avoid introducing parameters for adjusting T.
[b] Bennett et al. (1988), Brady and Walther (1990), House and Orr (1992).
[c] Kohler et al. (2003), Bibi et al. (2011), Suzuki-Muresan et al. (2011).
[d] Kamei and Ohmoto (2000), Kuechler and Noack (2007), Liu et al. (2008), Truche et al. (2010).
[e] Chou and Wollast (1985a, 1985b), Casey et al. (1991), Stillings and Brantley (1995).
[f] Malmstrom et al. (1996), Brandt et al. (2003), Black and Haese (2014).
[g] Kalinowski and Schweda (2007), Mareschal et al. (2009).
[h] Whittemore and Langmuir (1974), Yoshida et al. (2002).
[i] Brantley et al. (2007a).
[j] Kohler et al. (2003).
[k] Williamson and Rimstidt (1994), Kolowith and Berner (2002), Liermann et al. (2011).
[l] Chou and Wollast (1985a), Peucker-Ehrenbrink and Hannigan (2000).
[m] Peucker-Ehrenbrink and Hannigan (2000), Moore (2008).
[n] Kalinowski and Schweda (2007).

2.6. Evolution of soil chemistry and porosity

During chemical weathering, porosity evolved as a result of the reactions between the solid and aqueous phases. The loss or gain in mass for each mineral phase through dissolution and precipitation were related to changes in volume and porosity successively as per previous studies (Navarre-Sitchler et al., 2009; Li et al., 2010; Brunet et al., 2016; Wen et al., 2016). Briefly, CrunchFlow solved Eq. (1) to calculate species concentration and mineral phase mass changes. The mass changes were converted into volume changes using mineral molar volumes, which were then converted to mineral volume fractions in each grid block. The porosity at time t in each grid block g was calculated as follows:

$$\phi_{g,t} = 1 - \sum_{g=1}^{n} V_{g,j,t} \quad (4)$$

Here $\phi_{g,t}$ is the porosity in the grid block g at time t, n is the total number of mineral phases, and $V_{g,j,t}$ is the volume fraction of mineral phase j in grid block g at time t. Mineral surface areas were updated according to evolving mineral mass and the specific surface area (SSA). Dissolution and precipitation may change SSA by decreasing grain size, by increasing pore connectivity or by producing surface coatings (Navarre-Sitchler et al., 2009, 2013). These processes can change SSA in opposite ways and have not been investigated specifically for this soil. Our model therefore used a constant SSA and at each time step the model calculated the total surface area (A) of each mineral in each grid block as the product of SSA (m^2/g) and the new mineral mass (g). Over geological time scale, the shale rock lost mineral mass through outflow of dissolution products so that porosity increased from the original 6% to about 50% at 10k years. Correspondingly, the permeability increased significantly following the porosity-permeability relationship. We however assume constant (average) flow velocity from the net rainfall so total water mass going through the rock is constant. This is commonly done in other RTM studies for chemical weathering (Lebedeva et al., 2010; Moore et al., 2012), because the water flow into the soil represents the amount of the net infiltration.

2.7. Simulation conditions and model calibration

To model weathering of a black shale requires inclusion of organic matter oxidation, mineral reactions, biota, erosion, frost heave, climate change, and many more factors. No such all-inclusive models are available today. The intent of this modelling work was to assess weathering of the shale after oxidation of the organic matter had already occurred at depth. Thus, we constrain our model by (i) fitting the modern day pore water chemistry and (ii) reproducing the mineralogical depth profiles as observed today. We used pore water data collected at MRT and soil chemistry measurements at RT1. Soil chemistry of a secondary ridge top location (RT2) was also reported by Jin et al. (2013). RT1 and RT2 are similar in terms of trends but more data points were reported for RT1. Given the geologically short time scale of weathering (10,000 years since deglaciation, we make the simplifying assumption that the rates of erosion are comparable to those of uplifting so that soil profiles and reaction fronts are primarily determined by chemical weathering. We also assumed that weathering could be modelled as an iso-volumetric process. That is, although porosity changes during weathering, there is no compaction or expansion that leads to pore volume alteration.

The minerals included in the simulation were chosen based on (i) observations of putative parent samples and soil samples, (ii) inferences from weathering of nearby soils, (iii) availability of kinetic and thermodynamic data, (iv) practical considerations related to computational time. Indeed, it was not our intent to reproduce every observation made for the soil, but rather to develop a tractable model that would allow us to understand important features of weathering of a black shale.

Given these considerations, a simplified initial bedrock composition was used (Table 1) based on the rock samples collected at shallow depths. These samples were reported to contain ~40 wt% quartz, 2 wt% pyrite, up to 50 wt% clay (illite and chlorite), 4 wt% plagioclase, and <2 wt% rutile. We assumed that the organic matter had already been oxidized and removed from the rock, as described previously. Weathering of chlorite was assumed to produce vermiculite based on previous weathering studies and the nearby Rose Hill shale (Jin et al., 2010). Iron hydroxide (goethite) was observed as a secondary mineral and therefore was included in the model. We implicitly assumed that erosion during the LGM removed all regolith and bare bedrock was exposed at the time of initiation of weathering. An initial porosity of 6.0% was set throughout the column (Jin et al., 2013).

The amount of pyrite in the soil today is negligible compared to the amount of pyrite inferred to be present in the parent rock. However, the model showed that pyrite was only depleted by oxidative dissolution if $O_{2(aq)}$ was continuously present in the soil water. This observation is consistent with previous RTM simulations of weathering where the depths to reaction fronts and the reaction rates have been shown to strongly depend on the interaction of the pore fluid with $O_{2(g)}$ and $CO_{2(g)}$ (Bolton et al., 2006; Moore et al., 2012). Although we do not simulate multiphase flow dynamics here, we maintained a continuous presence of $O_{2(aq)}$ in the modelled pore fluids by using an imaginary mineral $O_{2(s)}$ that continuously released $O_{2(aq)}$ to maintain an equilibrium at $10^{-3.6}$ mol/l (8 mg/L) at all times. In addition, because modeling without including CO_2 showed calculated pH values were much higher than measurements, we included an imaginary mineral ($CO_{2(s)}$) that continuously released $CO_{2(aq)}$ to represent the acidity introduced by both CO_2(g) and organic acids (Drever and Stillings, 1997; Moore et al., 2012). Similar to the O_2 release, the CO_2 release was assumed fast. We have to maintain a $CO_{2(aq)}$ concentration of $10^{-2.10}$ mol/L in the model to reproduce data. This $CO_{2(aq)}$ concentration is much higher than the equilibrium concentration of $10^{-3.5}$–$10^{-3.2}$ mol/L at typical soil CO_2 pressure 1.02–2.0×10^{-2} atm (Hasenmueller et al., 2015). This is because the dissolved CO_2 (aq) was used to represent acidity introduced by both soil CO_2(g) and organic acids. The representation of organic acid using CO_2(aq) has some limitations.

Organic acids not only provide a source of acidity, but also a capacity for complexation that can alter mineral solubility (Neaman et al., 2005; Lawrence et al., 2014). This is not represented in the model when CO_2 is used without organic acids. Other effects of vegetation such as cycling of elements in the shallow soil are also not considered in the model.

The solid phase elemental compositional data and pH were reproduced first by adjusting the release rate of $CO_{2\,(aq)}$ into the pore water and the specific surface areas of dissolving minerals. Aqueous concentrations were then fit by adjusting flow velocity and the SSA of vermiculite. This is the only secondary mineral that takes up ions other than Fe from the soil water in our model and is thus an important constraint on pore water concentrations. In general, we found that reaction kinetics of primary minerals were also more important for reproducing the solid phase composition whereas the thermodynamics of secondary minerals (equilibrium constants that determine at what concentrations precipitation occurs) strongly controls aqueous chemistry.

2.8. Simulation cases for sensitivity analysis

We first calibrated a base case model to reproduce soil and aqueous compositions. The base case model was obtained by minimizing the sum of the square of the differences between the model output and data for all solid phases and aqueous species (Gupta et al., 1998). This base case simulation started with a parent composition with 6% porosity (Table 1) and average infiltration of 0.4 m/year, slightly lower than the 0.5 m/year based on mean annual precipitation and evapotranspiration (see discussion below). A sensitivity analysis was performed in 200 simulation runs to determine the key parameters that control weathering. Parameters such as diffusion and dispersion were found to have negligible impacts whereas specific surface area, flow velocity, and reactive gases were found to be important. As an example, for the effects of SSA, we compared the base case with two additional cases with 0.1× and 10.0× the SSA of the base case. The base case was also compared with two additional cases with high flow (HF, 4.0 m/year) and low flow (LF, 0.04 m/year). Effects of the reactive gases O_2 and CO_2 were examined in the base case model (labelled "CO_2&O_2") and three more cases including either one of the gases ("CO_2Only" and "O_2Only") or without either gas ("NoGas") (Table A3 in Supplementary Information). The mass balance of each simulation case was checked to ensure the correctness of the numerical calculation.

3. RESULTS

3.1. Pore water chemistry

Measured pore water chemistry is in Table B1 for all positions on the hillslope. Although we only modelled the ridgetop soil (MRT), observations in other landscape positions help define the system. The pH of soil water from 10 cm below the land surface varied between 3.7 and 4.2 (Fig. 1a). The values observed in the MRT site were on average about 0.4 units higher than those downslope (MMS, MVF). The pH increased with depth at all sampling locations; however, the specific trends varied among different sampling locations. The MRT pH remained close to 4.5 while the MMS values increased from about 3.7 to 4.7. Increasing pH with depth and with position downslope were consistent with ongoing weathering reactions.

The dominant aqueous anions were sulfate and chloride (Fig. 1b and c). Chloride concentrations were the lowest at MRT and highest at MMS. Sulfate concentrations remained relatively constant at MRT while increased with depth in the MVF and decreased at MMS. Other anions, including nitrate and fluoride, were present at relatively low concentrations (Tables B1 and B2). In general, most anions showed lower concentrations at MRT compared to MMS and MVF, consistent with increasing concentrations downslope. A reasonable explanation is that pore water mostly moves vertically as unsaturated flow; however, some pore water moves downslope along the hill due to periodic perched water conditions at the soil-bedrock interface. For this reason, we only modelled the MRT soil.

The dominant aqueous cations were Ca, Na, and K followed by Al and Mg. Concentrations of Na and Mg remained relatively constant with respect to depth. The Na concentrations were lowest at the MRT, which also had the highest Mg concentrations. The concentrations of K, Al, and Fe decreased consistently with depth. Such behavior can indicate mineral precipitation (likely for Al and Fe) or uptake into roots (likely for K). On a molar basis, silica concentrations were the highest among all species with a decreasing trend with depth at the MRT and an increasing trend at MMS and MVF. Overall, the variations of aqueous concentrations at different depths and sampling locations reflect the hydrogeochemical complexity at the hillslope scale.

3.2. The base case model

Here we first present the base case model that reproduces today's pore water and soil chemistry data (Fig. 2). The Al, Mg, and K increase rapidly with depth for the top 50 cm but remain nearly constant from 50 to 100 cm. Al comprises >6 wt.% of the soil at the surface and >9 wt.% at 50 cm. Fe, Na, and Si concentrations remain relatively constant with depth. The concentrations of S were measured to be negligible (0.005–0.018%, not shown) and constant with depth, consistent with complete pyrite depletion in the top 120 cm of soil. The measured porosity was 50% close to the surface, gradually decreasing to 40% at depth (Fig. 2g). The modeled porosity captured the trend of porosity change with depth but underestimated the actual values. This might be due to the assumption of isovolumetric changes. In natural systems, porosity is also altered by physical and biological processes, such as compaction and root growth that change the pore volume. Jin et al. (2013) reported volumetric strain such that shallow soils were expanded and deeper soils were slightly collapsed.

Fig. 3 compares the soil water chemistry data (from the lysimeter nest at MRT) and the model output. Concentrations

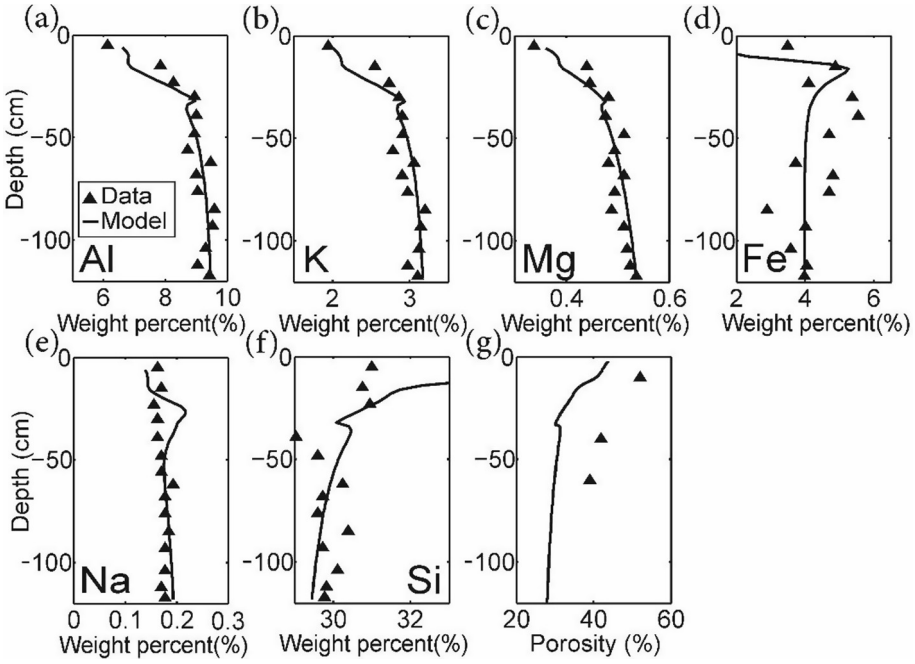

Fig. 2. Comparison of model output (line) and measurements (symbols) at RT1 at the current time (10k years). Al, K, and Mg are present in (dissolving) illite and chlorite and (precipitating) vermiculite (Table B4). Iron is present in pyrite, illite, chlorite, and goethite. The porosity data were derived from measurements at MRT. The elemental composition has a relative error of ±5% that fall within the symbols.

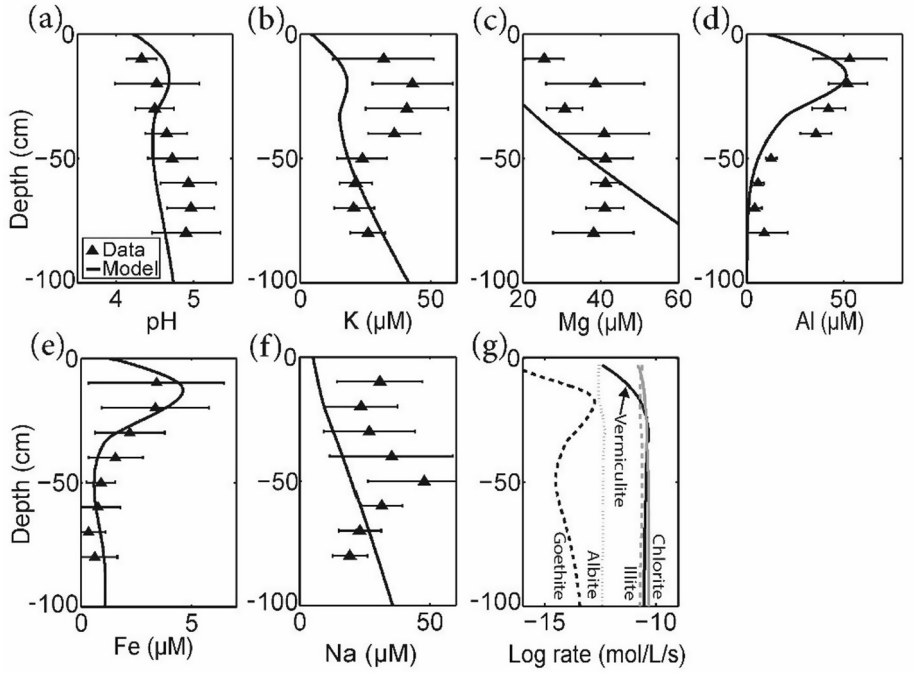

Fig. 3. Comparison of data (symbols) and model output (lines) at the ridgetop site MRT at the current time (10k years) for (a) pH, aqueous concentrations of (b) K, (c) Mg, (d) Al, (e) Fe, and (f) Na, and (g) mineral reaction rates (mol/L bulk volume/s). The increases in aqueous concentrations in the top 30 cm in the model are generally due to dissolution of chlorite and illite (both of which consume H^+). Between 30 cm and 50 cm, vermiculite precipitates and pH decreases. Concentrations of Al, K, Mg and Fe vary depending upon the dissolution or precipitation at each depth. Deeper than 50 cm, the concentrations of all species and pH increase with depth due to the slight dominance of chlorite and illite dissolution over vermiculite precipitation (g).

of Al, K and Mg were observed to be considerably higher than Fe. Concentrations of Na and Mg remained relatively constant versus depth while those of other elements generally increased with depth. The pH values increased from 4.3 in the rainwater to 4.7 at 30 cm. Between 30 cm and 50 cm, the pH values decreased to a minimum of 4.3 at 50 cm. Similarly, concentrations of K, Al, and Fe increased with depth. Deeper than 50 cm, all species changed only slightly with depth, indicating the most active zone in the top 50 cm of soil. We do not show modeled anions such as Cl and SO_4. This is because no reactions in the modelled geochemical reaction network (Table 1) would change these anions at the present time, because Cl is a tracer and pyrite is depleted. As such, in the 'homogeneous soil column" that we simulated, the modeled Cl and SO_4 concentrations were the same as the inlet concentrations from the rain. We believe the spatial variations in Cl and SO_4 concentration data (Fig. 1) are likely caused by the dynamics of the hydrological conditions (ups and downs of hydrological conditions), the spatial heterogeneities such as preferential flow paths, as well as possible microbe-mediated reactions. These details are not represented in the current model.

The solid and aqueous concentrations reflected the chemistry at the present time where pyrite has become depleted and chlorite is the main dissolving mineral and vermiculite is the main precipitating mineral (Fig. 3g). The dissolution of chlorite and illite consume $H^+$and release Al, K, Mg, and Fe, while precipitation of vermiculite and goethite are the only precipitates incorporating the latter 4 elements. This explains the generally increasing or constant aqueous concentrations versus depth. At approximately 30 cm, the solution becomes over-saturated with respect to vermiculite and Fig. 3g shows that

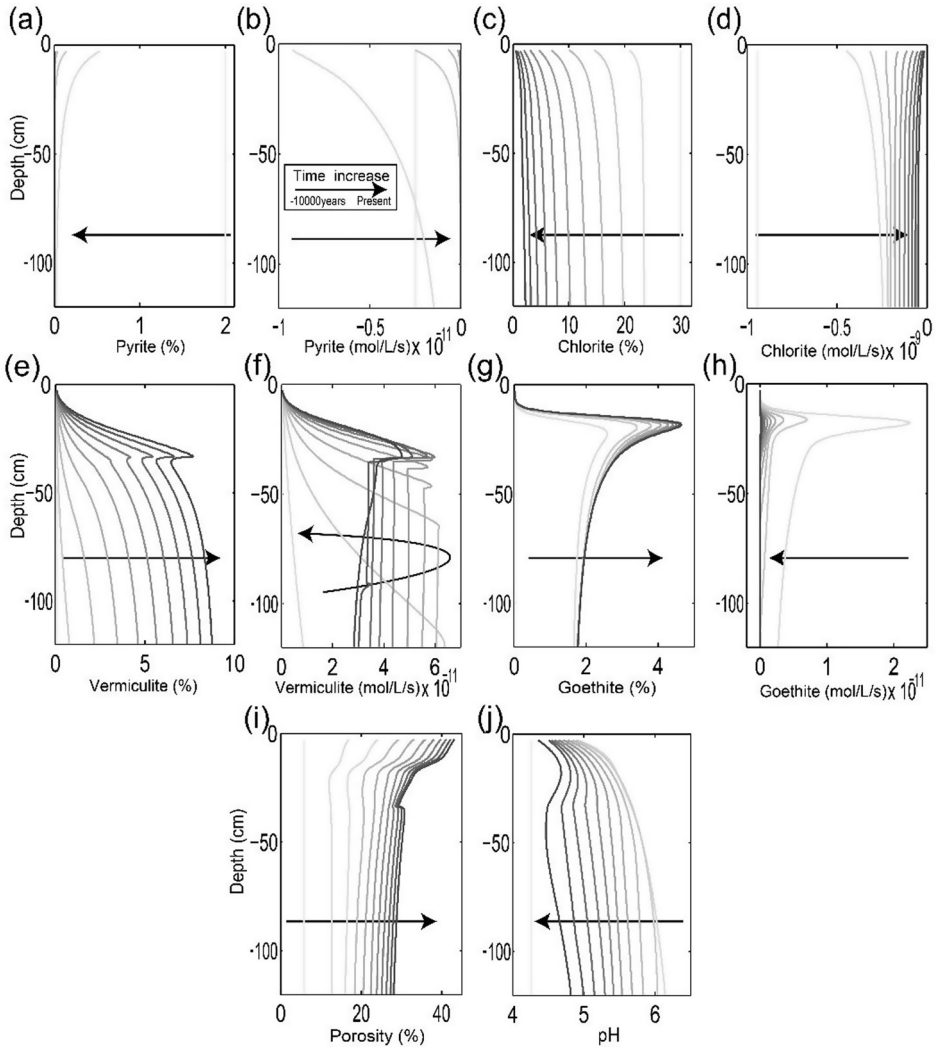

Fig. 4. The modelled evolving depth profiles of (a) pyrite, (c) chlorite, (e) vermiculite, (g) goethite, and (i) porosity; and modeled reaction rates (mol/L bulk volume/s) for (b) pyrite, (d) chlorite, (f) vermiculite, (h) goethite, and (j) predicted pH. The curves show progress from the lightest gray at the initiation of weathering to the darkest gray for the present time (time interval between curves = 1000 years). Pyrite was depleted almost completely within the first 1000 years (and so only a few gray curves are shown) and was accompanied almost entirely by goethite precipitation. Porosity evolved as a result of mineral volume fraction (i.e., the volume fraction of minerals + porosity was constrained to equal 100%). The black arrow indicates the direction of the evolution from 10,000 years ago to the present time.

vermiculite precipitation rate reaches its maximum at 30 cm. Vermiculite precipitation reduces the aqueous concentrations of Al, K, Mg, and Fe and releases H^+. Iron is solubilized during dissolution of pyrite, illite, and chlorite, and precipitates as goethite or vermiculite. Albite is the only Na-containing mineral in the model. The observed Na concentrations do not change significantly with depth; however, the model predicts a continuous increase in Na concentration with depth because albite continues to dissolve without precipitating. The data-model discrepancy potentially indicates another sink for Na such as sorption or ion exchange, which is not included in the model.

Fig. 4 shows the temporal evolution of mineral volume fractions and reaction rates. Pyrite dissolved rapidly and was completely depleted within the first 2000 years (Fig. 4a). This pyrite dissolution was accompanied by low pH (~4.1) in soils and pore waters, consistent with release of H_2SO_4 during oxidative dissolution of pyrite. After 1000 years, pH increased dramatically at 2000 years to a maximum of 6.0 (Fig. 4j). Correspondingly, chlorite dissolved fast in the first 1000 years and slowed significantly after that. After 2000 years, chlorite dissolution continued to decrease corresponding to its volume fraction decrease from 35% to 2% (Fig. 4b). Although not shown here, illite dissolution slowed over time as its volume fraction decreased by about 2% over 10k years.

Vermiculite and goethite were the major precipitating minerals and the major Fe sink: their relative importance switched before and after pyrite depletion (Fig. 4e and g). Specifically, within the first 1000 years, goethite precipitated with negligible vermiculite precipitation due to high concentrations of Fe(II). After 1000 years, vermiculite became the major sink for dissolved Fe: this occurred because of the lower Fe(II) concentrations and higher pH after pyrite depletion. Over time, the spatial distribution of vermiculite followed that of pH closely, i.e., the vermiculite precipitation front moved upward with time, from the deeper higher-pH soil toward the surface until it reached ~30 cm after 10k years of weathering. As chlorite dissolved, vermiculite precipitated. Because chlorite dissolution rates decreased over time, precipitation of vermiculite also diminished with time. The tendency for vermiculite to precipitate in the deeper soil led to the formation of lower porosity in the deeper soil. Thus, the porosity essentially mimicked the vermiculite volume fraction in reverse (Fig. 4e and i). Porosity in the base case model increased from the initial value of 6 to ~45% at the top of the column and close to 30% at the bottom (Fig. 4i), consistent with field measurements.

Fig. 5a shows a schematic of important reactions and the role of reactive gases (O_2 and CO_2). Chlorite dissolution released cations that in turn precipitated as secondary vermiculite and goethite. Pyrite reacted with O_2 and released Fe. The Fe from pyrite and chlorite dissolution reacted with O_2 and precipitated as goethite. Chlorite dissolved about two orders of magnitude faster than illite for the first 1000 years. As illustrated in Fig. 5b, this rate difference slowly diminished over time, reaching rates that were very similar at the present time (mostly because of the continuous decrease in chlorite abundance). Pyrite dissolved rapidly and was depleted within the first 1000–2000 years. Correspondingly, goethite precipitation dominated over the first 1000–2000 years, whereas vermiculite precipitation dominated after 2000 years (Fig. 5c). The rate of goethite precipitation of goethite decreased after 1000 years while that of vermiculite increased until reaching its maximum at about 5000 years. After 5000 year, the vermiculite precipitation rate decreased as chlorite dissolution slowed due to diminishing mineral mass.

Two distinct stages of porosity increase can be identified (Fig. 5d). The initial stage of fast increase lasted almost 1000 years during rapid pyrite dissolution. The dissolution

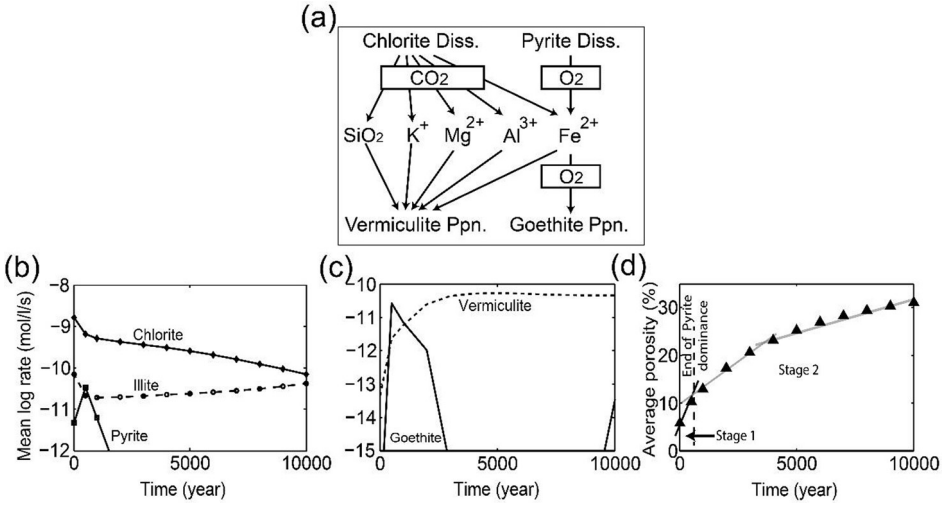

Fig. 5. (a) Schematic of the dominant reactions highlighting the roles of O_2 and CO_2 gases in controlling weathering. The figure emphasizes that interaction of $H_2O + CO_2$ with chlorite releases Si, KI, Mg, Al, and Fe, which in turn leads to vermiculite precipitation. Pyrite oxidation also releases Fe(II) which then oxidizes and precipitates as goethite but is also incorporated into vermiculite. Reaction rates were averaged over the whole column and plotted versus time for (b) dissolving and (c) precipitating minerals. (d) The predicted stages of weathering shown for porosity versus time.

maintained acidic conditions, accelerated chlorite dissolution, and was responsible for the steep porosity increase. The next stage started after pyrite depletion: during that stage, chlorite dissolution drove the porosity increase. Compared to the first stage, more vermiculite was precipitated, which partly compensated for the porosity increase related to loss of chlorite. The porosity increase in the second stage slowed after about 6000 years because the chlorite dissolution rate slowed significantly.

3.3. Sensitivity analysis

Sensitivity of the calculated weathering processes to different parameters was analyzed. The weathering processes depend most strongly on specific surface area, flow velocity, and the presence of $CO_{2(g)}$ and $O_{2(g)}$. Among these, the key parameters controlling the weathering are the mineral surface areas of chlorite and vermiculite. Details of important parameters are in Table A3 in Supplementary Information.

3.3.1. Specific Surface Area (SSA)

Reaction rates measured in well-mixed batch experiments have been shown to be 2–5 orders of magnitude higher than those measured in field studies (Swoboda-colberg and Drever, 1993; White, 1995; White and Brantley, 2003; Navarre-Sitchler and Brantley, 2007; Luttge et al., 2013; Reeves and Rothman, 2013). This discrepancy has hindered the use of laboratory-measured rates in predicting processes in natural subsurface systems. In reproducing data in the base case here, we reduced the specific surface area for some of the reactive minerals (chlorite, vermiculite, pyrite, and goethite) up to five orders of magnitude compared to specific surface area values measured by BET and reported in the literature for mineral powders (Table 1). This is not surprising compared to other studies of reactive transport modelling of natural systems (Li et al., 2017a; Moore et al., 2012). This indicates: (i) soil mineral surface area is not comparable to mineral powder surface area, and (ii) not all of the surface area of the reacting minerals is "accessible" to non-equilibrated water.

The lack of accessibility might be attributed to the presence of secondary clay precipitates that armor surfaces (Nugent et al., 1998) and physical and chemical layering or clustering of reactive phases. Various studies have also used imaging techniques and X-ray neutron scattering to show that the accessible fraction of surface area can vary between 5% and 39% of total mineral surface areas (Peters, 2009; Landrot et al., 2012; Beckingham et al., 2016; Gu et al., 2016). Sometimes, accessibility of non-equilibrated water is limited to a few major conductive flow

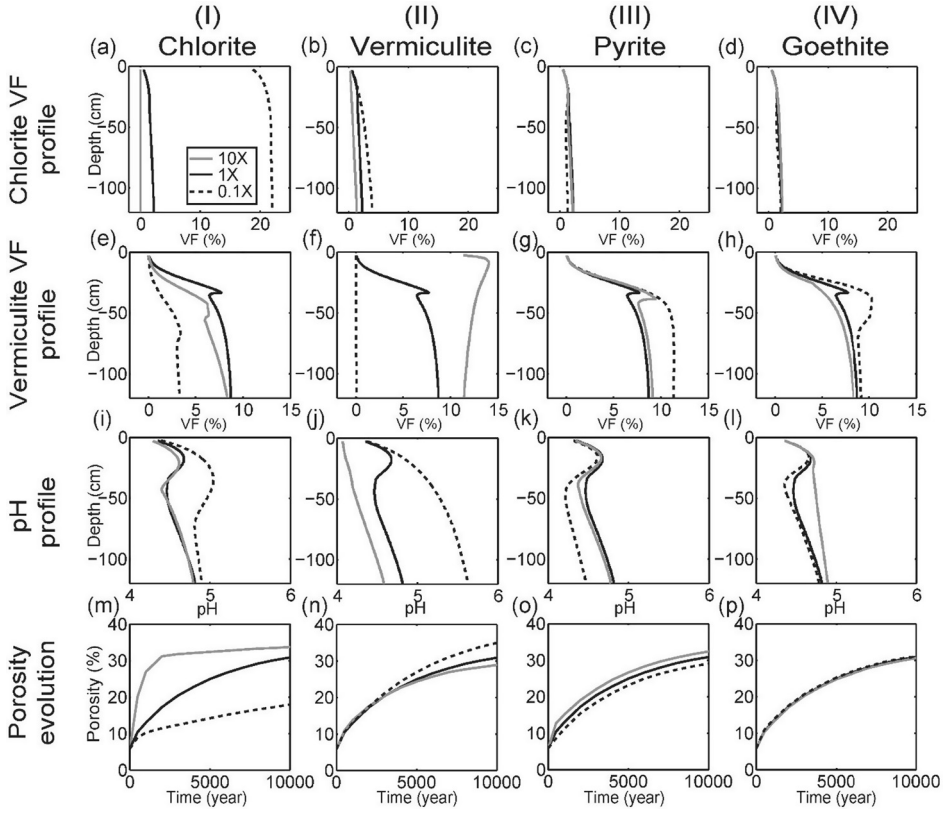

Fig. 6. Effects of changing SSA: SSA was varied from the value in the base case (noted as 1×), to 10 times of base case (noted as 10×), to 10 times lower than the base case (0.1×). Changing chlorite SSA is shown in column I, vermiculite SSA in column II, pyrite SSA in column III, and goethite SSA in column IV. The first three rows show the spatial profiles of volume fraction (mineral volume/ soil volume) of chlorite and vermiculite, and pH; the last row shows the average porosity change over 10k years.

pathways in heterogeneous porous media (Zachara et al., 2016). In addition, not all accessible surface area is effectively dissolving. For example, a mineral that does not have any coating and is accessible through connected pore structure can be bathed in a fluid at equilibrium in the low permeability zone of a heterogeneous medium and therefore it is not effectively dissolving (Molins et al., 2012, 2017; Li et al., 2014; Salehikhoo and Li, 2015; Wen et al., 2016). In natural systems, all these factors can operate simultaneously resulting in much smaller effectively-dissolving surface areas than the measured BET or imaged surface area. The dominance of different factors may vary under different mineralogical and flow conditions. Nonetheless, our modelling demonstrated that TST rate laws can be used in a reactive transport model to simulate weathering processes after reducing SSA of the reactive minerals by orders of magnitude.

For the sensitivity test, the SSA of chlorite, vermiculite, pyrite, and goethite were varied over two orders of magnitude in three demonstration runs. Specifically, the SSA of each mineral was decreased or increased by 10 times while all other values of SSA were held the same as the base-case values. In this way, we sought to identify the effect of SSA choices for the most important minerals that control the weathering process. Fig. 6 compares four sets of numerical experiments. A change of SSA for either chlorite or vermiculite significantly impacted the evolution of both the chlorite and vermiculite volume fractions. After 10,000 years, chlorite was either completely dissolved (a 10× increase in SSA), or was depleted with only 2% remaining (1×, base case), or depleted with 22% remaining (0.1×) (Fig. 6a). Similarly, vermiculite precipitated much more in the 10× vermiculite SSA case (13%), compared to 7% and 0% in the base case and 0.1× SSA case (Fig. 6f). As a result, the porosity increased rapidly in the 10× chlorite SSA case to almost 30% over the first 2000 years while that of the lower SSA case increased less than 10% over 10,000 years (Fig. 6m). A change in the vermiculite SSA did not greatly affect chlorite volume fraction however led to precipitation of much more vermiculite. The extent of porosity evolution, however, was relatively small (~7%) (Fig. 6n) compared to more than 15% in chlorite SSA cases (Fig. 6m). This indicates that although vermiculite precipitation regulates aqueous solution compositions and pH, it plays a minor role compared to chlorite dissolution, the primary driving force for chemical weathering.

A decrease in the pyrite SSA (0.1×) did not change the volume fraction of chlorite by much (Fig. 6c); however, it did increase the pH and facilitated vermiculite precipitation (Fig. 6g and k). This in turn led to opening of 5% less porosity compared to the 10× high pyrite SSA case (Fig. 6o). An increase in goethite SSA resulted in negligible

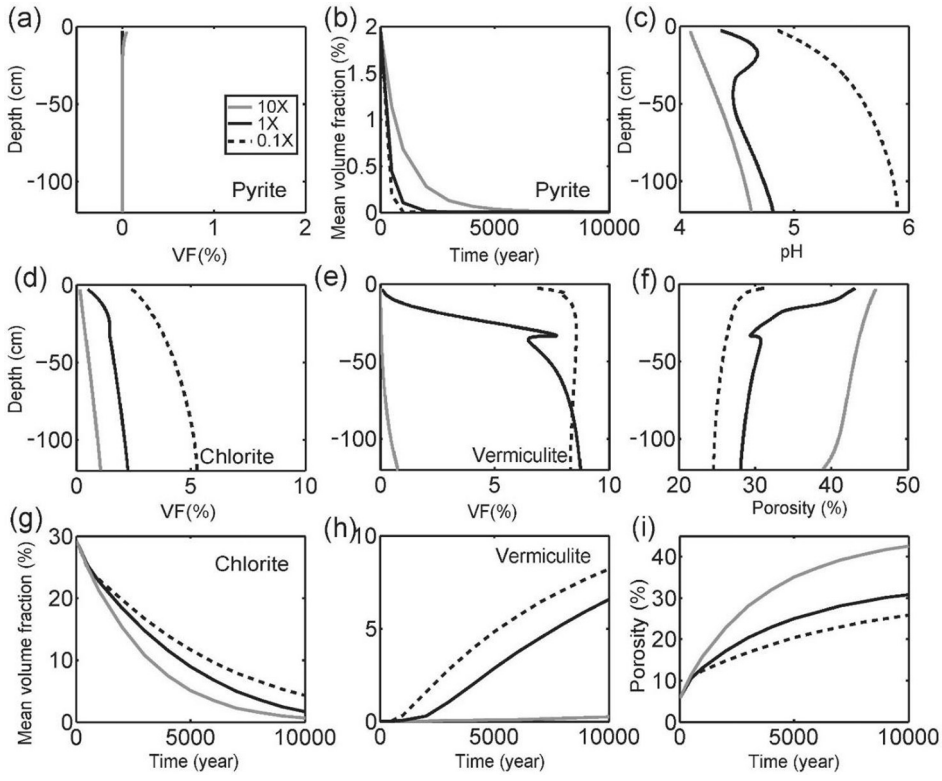

Fig. 7. Effects of flow velocity on the volume fraction (i.e., volume %) of minerals in sensitivity tests with high flow (4.0 m/year, i.e., 10× the base-case flow), base-case flow (0.4 m/year, labelled 1×), and low flow (0.04 m/year, labelled 0.1×): profiles at 10k year of (a) pyrite, (c) pH, (c) chlorite, (d) vermiculite, and e) porosity; temporal evolution of profiles of (b) pyrite, (g) chlorite, (h) vermiculite, and (i) porosity. Aqueous pH strongly depends on flow velocity. Faster flow leads to faster chlorite dissolution and flushing of dissolution products, resulting in less vermiculite precipitation and lower pH.

changes in chlorite; however, it led to less vermiculite precipitation because goethite and vermiculite competed for the dissolved Fe. This in turn increased pH because ions were not precipitating out of solution as vermiculite. At the end, however, the decrease in vermiculite volume fraction was compensated by an increase in goethite volume fraction, leading to essentially the same porosity (Fig. 6p).

In general, changes in the SSA of primary minerals (chlorite and pyrite) exert a stronger control than changes in SSA of the secondary minerals (goethite, vermiculite) on the porosity depth profiles. However, secondary mineral precipitation (vermiculite and goethite) determines the extent of accumulation of dissolved ions in water and therefore impacts pH.

3.3.2. Flow velocity

The mean annual rainfall in Pennsylvania is ~1 m. Given that about half of the rainfall is lost to evapotranspiration, the maximum amount of water that could enter the soil is ~0.5 m/year. However, this estimate has considerable uncertainty over 10k years and over seasons. As such, we used flow velocity as a fitting variable. The flow velocity of 0.4 m/year best reproduced the data (base case). One explanation for this slightly low value might be that 0.1 m/year is lost as surface runoff that does not interact with the weathering rock, which is actually close to the surface runoff in the Shale Hills watershed that is about 30 miles away (Li et al., 2017a).

Here we analyze the role of flow velocity by changing the flow velocity by two orders of magnitude from the base case. Fig. 7 compares the predicted mineral composition profiles at the present time for the high-flow (HF, 4.0 m/year), base-case (BC, 0.4 m/year), and low-flow (LF, 0.04 m/year) simulations. Fig. 7a illustrates that in all three cases, pyrite was almost depleted in the top 120 cm of soil. Pyrite dissolution was thermodynamically favorable and occurred under far from equilibrium conditions. However, somewhat counterintuitively, pyrite lasted longer in the HF cases. This is because water is more acidic in the HF case and pyrite dissolution rates inversely depended on acidity (Fig. 7b and c). The pH was lower in the HF case due to lower residence times and less reaction with chlorite and faster flush of chlorite dissolution products. Compared to the large difference in the chlorite remaining after 10,000 year (0% versus 20%) using differing SSA values, the remaining chlorite only varied from 1% to 4% in the HF and LF cases, respectively (Fig. 7d).

The effect of flow rate was much more pronounced for vermiculite (Fig. 7e). Vermiculite was observed to precipitate only slightly (<1% volume fraction in the deep soil column) in the HF case while it reached 7% in the LF case due to the much slower flushing rates of the chlorite dissolution products. Overall, under conditions of HF, more chlorite dissolved and less vermiculite precipitated, resulting in almost 20% higher porosity in HF compared to LF at 10,000 years (Fig. 7i). These variations in flow velocity

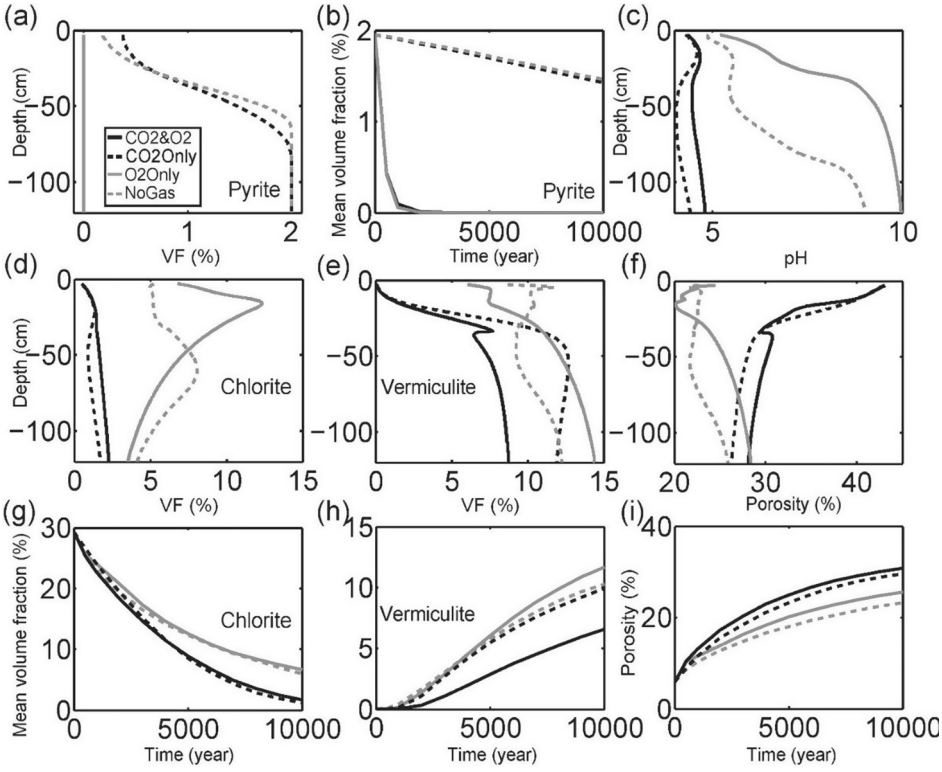

Fig. 8. Comparison of four cases with and without CO_2(aq) and O_2(aq) in the soil (Table A3). Spatial profiles of (a) pyrite, (c) pH, (d) chlorite, (f) porosity, and (g) the mean volume fraction (VF%) evolution of (b) pyrite, (g) chlorite, (h) vermiculite, and (i) porosity.

resulted in relatively large variations in the porosity profiles. One inference from this (and from the observation in the previous figure that porosity profiles at 10k years do not vary as much with SSA) is that the porosity of a weathered profile may be used to tune the flow velocity for an RTM.

3.3.3. Reactive Gases

The role of reactive gases (O_2 and CO_2) is shown in Fig. 8 with four cases: the base case with the presence of CO_2 and O_2 (CO_2&O_2) and three more cases including either one of the gases (CO_2 Only and O_2 Only) or no gases (NoGas) (Table A3). In particular, pyrite depletion and soil elemental data can only be reproduced when both O_2 and CO_2 gases are present in the column. Note that "no gases" and "CO_2 only" do not mean there is no O_2 in the system at all. Rather, it means that we did not include O_2(s) that would have provided O_2 to the system throughout the simulation. In cases without O_2(s), O_2(aq) is always present in the incoming rainwater; therefore, in those simulations, pyrite still dissolves, although at much lower rates due to the limited O_2. Oxygen is essential for pyrite oxidative dissolution and precipitation of goethite. In the two cases without O_2, for example, the pyrite reaction front only penetrated 60–75 cm over 10k years. The average volume fraction of pyrite remaining at depth equaled 1.5% after 10k years (Fig. 8a and b). Although O_2 has a strong impact on the dissolution of pyrite, the small pyrite volume fraction (2%) results in a relatively small impact on the long-term development of porosity. Without CO_2, O_2 changed the local shape of chlorite dissolution; however, it did not affect overall chlorite dissolution to a great extent (Fig. 8d and g).

In contrast to O_2, the effects of soil CO_2 on pyrite dissolution are relatively minor. The pyrite dissolution front for the CO_2Only case is only slightly deeper than the NoGas case. Carbon dioxide (which we include also as a proxy for organic acids) controls the pH after pyrite depletion. For silicates, the presence of CO_2 in general led to much more acidic conditions (Fig. 8c). This in turn facilitated more chlorite dissolution and less vermiculite precipitation (Fig. 8d, e, g, and h). More chlorite dissolution and less vermiculite dissolution led to a larger porosity increase in the presence of CO_2 (Fig. 8i).

4. DISCUSSION

4.1. Model limitations

Like all models, the RTM here did not treat many aspects of weathering. It is most useful as a tool to understand net processes rather than as an exact simulation of weathering. For example, we did not include the effect of volume change during weathering as reported by Jin et al. (2013) nor did we include some of the complexities of the mineralogical changes. Likewise, we only assumed simple TST-like reaction rate laws and we did not explicitly include biological effects. We also did not include organic matter – ancient or modern – in the model.

Even though the model did not incorporate all factors, the simulations yielded many robust conclusions about the weathering process, including the importance of pyrite oxidation, flow velocity, and reactive gas concentrations. Our model documented that pyrite oxidation occurred very early during weathering. We implicitly included the effects of organic acids released from decomposition of ancient and modern organic matter by including aqueous CO_2 (carbonic acid) as a source of protons. Furthermore, since Jin et al. (2013) argued that at least half of the sedimentary organic matter (OM) oxidized to some extent before the depth of refusal to hand augering, we assumed that the deep oxidation of OM presumably did not need to be included in our RTM since we focused only on the upper ~100 cm. In effect, we assume that the depth of organic matter depletion from the parent bedrock is deeper than our simulation and the removal of organics occurred before soil formation.

4.2. Key controls of black shale weathering

Our observations and modelling are not discrepant from the one RTM model in the literature for weathering of black shale (Bolton et al., 2006). Unlike our efforts, that team modeled both oxidation of pyrite and OM in a soil column developed on black shale and compared it to observations (Wildman et al., 2004). They reported that the pyrite weathering front occurs at a similar depth to that of organic matter although the pyrite front was much sharper than the OM weathering front. Neither Mathur et al. (2012) nor Jin et al. (2013) explicitly report the depths of the weathering fronts of OM and pyrite because these fronts were both inferred to be deeper than the depth of sampling (limited by hand augering). However, Jin et al. (2013) suggested that one half or more of the OM was oxidized from the Marcellus sites beneath the zone of sampling, whereas pyrite was almost 100% depleted beneath the sampling zone. Therefore, it is possible that, like the Bolton et al. (2006) observations, the fronts for pyrite and OM are at similar depths in the Marcellus although the pyrite front is sharper. This suggests that pyrite may be more reactive in the surface environment than the ancient OM.

In fact, to simulate observations, both our model and that of Bolton et al. (2006) had to include O_2 for a continuous presence of oxygen in the soil column to allow pyrite oxidation. Indeed, in our model where we assumed that no O_2 limitation occurred, pyrite was depleted within about 1000 years over the upper 120 cm. If we extrapolate this rate over 10 ky, we calculate a depth of 12 m for the pyrite reaction front. This inference is not inconsistent with the pyrite dissolution front that has been observed deeper than 20 m in the nearby Rose Hill shale at a ridgetop (Brantley et al., 2013). In that shale, the starting material has lower pyrite content than the Marcellus, perhaps explaining the extremely deep oxidation front. We conclude that the role of O_2 is significant in the early stage of shale weathering before pyrite depletion. Because pyrite only occupies 2% volume fraction, however, the time duration over which O_2 is important is relatively small and its impact on the evolution of mineral composition and porosity development is limited. Of course, the effect of pyrite oxidative weathering

is expected to be important at some depth deeper than we sampled – i.e., at the depth of the pyrite oxidation front. After the early stage of pyrite depletion, the importance of CO_2 increased. In fact, we have to include a continuous source of acid in the model to reproduce weathering observations. The presence of a CO_2 source resulted in an additional average 8% in porosity compared to cases without CO_2.

Our analysis also revealed the effects of specific surface area and flow velocity. Among these, changes in the specific surface area of highly reactive minerals including chlorite, vermiculite, and pyrite induced the largest impacts on both aqueous and solid phase elemental composition. The sensitivity analysis showed that a decrease in SSA of chlorite by an order of magnitude from the base-case value reduced the porosity increase from 25% to only 10%. In general, changing SSA of the primary minerals (chlorite and pyrite) exerts a stronger control because they are the driving force of the weathering processes. Secondary mineral precipitation (vermiculite and goethite) determines the extent of accumulation of dissolved ions in water and therefore alters water chemistry and pH. However, compared to primary minerals, these secondary minerals exhibit a second-order control on the overall weathering progress.

We were only able to reproduce field measurements if we used very low specific surface areas of the reactive minerals: indeed, our values were up to six orders of magnitude smaller than values measured in the laboratory for separates of mineral powders. We infer that a high fraction of mineral surface area is not dissolving in the field system because of armoring, particle size, or lack of homogeneous flow of non-equilibrated porefluid in soils. The best-fit for the specific surface area for each mineral was different. For example, the best fit specific surface area for chlorite was 0.8 m^2/g in comparison to the range of 1.1–7.7 m^2/g reported in laboratory measurements of powders (Malmstrom et al., 1996; Brandt et al., 2003; Black and Haese, 2014). In contrast, the best-fit SSA of vermiculite was 9.0×10^{-6} m^2/g as compared to the laboratory values of 7.3×10^{-1}–1.74×10^{1} m^2/g (Kalinowski and Schweda, 2007; Mareschal et al., 2009).

In general, the need to use smaller SSA values than expected based on laboratory experiments is consistent with other studies of mineral dissolution (Moore et al., 2012; Salehikhoo et al., 2013; Li et al., 2014). Salehikhoo and Li (2015) summarized a series of well-controlled experiments examining the role of fluid velocity and chemical and physical heterogeneities in columns of reactive magnesite + inert quartz. They found that the effective dissolving surface area of magnesite, defined as the area of mineral surface bathed in solutions with $IAP/K_{eq} < 0.1$, had to be reduced by 1–3 orders of magnitude lower than measured BET surface area for mineral powders in order for a RTM simulation to match measurements. The extremely small SSA values for vermiculite in the base case model may also be related to the complexity of dissolution reactions that are not included in the model for illite and chlorite, and the complexity of modelling both dissolution and precipitation for vermiculite and its intermediates.

In addition, the work also highlights the importance of flow velocity. Lower flow velocity resulted in less chlorite dissolution and more vermiculite precipitation, which ultimately reduced the extent of porosity increase over the 10k years of weathering. This underscores the role of water residence time in determining water-rock interactions in literature (Brunet et al., 2016; Wen et al., 2016). In fact, a recently developed upscaled rate law in heterogeneous subsurface indicates that the key determinant of mineral dissolution rates is the contact time between reacting minerals and water (Wen and Li, 2017). Broadly, this emphasize the important role of climate and hydrological regimes in driving weathering processes.

5. CONCLUSION

In this work, we developed an RTM to understand the key controls on Marcellus shale weathering with constraints from soil and pore water data. Our modeling reveals two distinct stages over the 10,000 years of weathering that are recorded in the 120 cm soil column. According to the model, pyrite dissolution during the first 1000 years of soil genesis released considerable H^+. This acidification enhanced the dissolution of chlorite and precipitated over 2 vol.% of goethite. After pyrite depletion, the main source of acidity was aqueous CO_2, included in the model to take into account the presence of soil atmosphere CO_2(g) and to act as a proxy for the contribution of organic acids. During the remaining years of the simulation, chlorite dissolution slowed down due to the loss of surface area over time; 10 vol.% vermiculite precipitated, and goethite precipitation was negligible.

Our analysis emphasized the importance of specific surface area, flow velocity, and availability of CO_2 and O_2 gases in controlling regolith development. The best-fit values of the specific surface areas for chlorite and vermiculite were 1–3 orders of magnitude less than laboratory measurements on mineral powders. The observed pyrite depletion cannot be reproduced without the continuous presence of O_2. The acidity introduced by CO_2 in the model maintains the high chlorite dissolution rates and the corresponding rates of transformation into vermiculite.

Globally, shale formations account for 25% of continental lithologies (Suchet et al., 2003). Mineral dissolution from shales releases elements important for plant growth including Ca, K, and P (Huntington, 2000). Models such as the one we present here can be implemented to simulate weathering of shale formations and flux of nutrients into oceans and ecosystems in the Critical Zone, the zone that sustains life (Brantley et al., 2007b). The reaction network during natural weathering in the shallow subsurface is likely to be similar to weathering of Marcellus Shale drill cuttings (Barry and Klima, 2013; Phan et al., 2015). The reactions should also be somewhat similar to water-rock interaction in the deep subsurface during fracturing and natural gas production where external fluids are injected into Marcellus Shale gas reservoirs. We expect that pyrite will dissolve much slower at depth because O_2 is typically

removed before the injection of hydraulic fracturing fluids to prevent corrosion, the growth of bacteria, and sulfate mineral precipitation. Nonetheless, the RTM results reported here can be interpreted to clearly emphasize the importance of controlling O_2 to limit the onset of pyrite oxidation in deep water-shale reactions and the formation of barite as precipitates. However, validating an RTM is practically impossible for the deep subsurface. We argue that efforts to model low-temperature shale reactions, such as discussed in this paper, lead to greater confidence in modelling the same water-rock reactions at high temperature, pressure, and salinity conditions in deep subsurface. With reasonable extrapolation of equilibrium constants and rate constants under relevant conditions, our model could thus be implemented to understand water-rock interaction in engineered subsurface systems. This would allow the understanding and quantification of processes important in environmental risk assessment, including heavy metal release, among other concerns such as high salinity and complex organic compounds during Marcellus shale gas production.

ACKNOWLEDGEMENTS

This work was supported by The Pennsylvania Water Resources Research Center (PA-WRRC) and the National Science Foundation to LL (EAR-1452007). Financial assistance for the soil sampling and characterization was provided by National Science Foundation funding for the Susquehanna Shale Hills Critical Zone Observatory (EAR-07-25019 to C. Duffy, and EAR 12-39285 and EAR 13-31726 to S.L. Brantley). The authors appreciate the extended XRD analysis by Ashlee Dere on Marcellus parent rock and soil samples. We acknowledge three anonymous reviewers and the Associate Editor Dr. Brian Stewart for their careful reading and constructive reviews that have improved the manuscript.

SUPPLEMENTARY MATERIAL

The supplementary information includes the simulation scenarios in sensitivity analysis, and pore water and soil chemistry data for the Marcellus Shale. Supplementary data associated with this article can be found, in the online version, at http://dx.doi.org/10.1016/j.gca.2017.08.011.

REFERENCES

Armatas G. S. (2006) Determination of the effects of the pore size distribution and pore connectivity distribution on the pore tortuosity and diffusive transport in model porous networks. *Chem. Eng. Sci.* **61**, 4662–4675.

Balashov V. N., Engelder T., Gu X., Fantle M. S. and Brantley S. L. (2015) A model describing flowback chemistry changes with time after Marcellus Shale hydraulic fracturing. *AAPG Bull.* **99**, 143–154.

Barry B. and Klima M. S. (2013) Characterization of Marcellus Shale natural gas well drill cuttings. *J. Unconventional Oil Gas Resour.* **1–2**, 9–17.

Beckingham L. E., Mitnick E. H., Steefel C. I., Zhang S., Voltolini M., Swift A. M., Yang L., Cole D. R., Sheets J. M., Ajo-Franklin J. B., DePaolo D. J., Mito S. and Xue Z. (2016) Evaluation of mineral reactive surface area estimates for prediction of reactivity of a multi-mineral sediment. *Geochim. Cosmochim. Acta* **188**, 310–329.

Bennett P. C., Melcer M. E., Siegel D. I. and Hassett J. P. (1988) The dissolution of quartz in dilute aqueous-solutions of organic-acids at 25 °C. *Geochim. Cosmochim. Acta* **52**, 1521–1530.

Bibi I., Singh B. and Silvester E. (2011) Dissolution of illite in saline-acidic solutions at 25 °C. *Geochim. Cosmochim. Acta* **75**, 3237–3249.

Black J. R. and Haese R. R. (2014) Chlorite dissolution rates under CO_2 saturated conditions from 50 to 120 °C and 120 to 200 bar CO_2. *Geochim. Cosmochim. Acta* **125**, 225–240.

Bolton E. W., Berner R. A. and Petsch S. T. (2006) The weathering of sedimentary organic matter as a control on atmospheric O-2: II. Theoretical modeling. *Am. J. Sci.* **306**, 575–615.

Brady P. V. and Walther J. V. (1990) Kinetics of quartz dissolution at low temperatures. *Chem. Geol.* **82**, 253–264.

Brandt F., Bosbach D., Krawczyk-Barsch E., Arnold T. and Bernhard G. (2003) Chlorite dissolution in the acid pH-range: a combined microscopic and macroscopic approach. *Geochim. Cosmochim. Acta* **67**, 1451–1461.

Brantley S., Kubicki J. and White A. (2007a) *Kinetics of Water-Rock Interaction*. Springer.

Brantley S. L. (2010) Weathering rock to regolith. *Nat. Geosci.* **3**, 305–306.

Brantley S. L., Goldhaber M. B. and Ragnarsdottir K. V. (2007b) Crossing disciplines and scales to understand the critical zone. *Elements* **3**, 307–314.

Brantley S. L., Holleran M. E., Jin L. X. and Bazilevskaya E. (2013) Probing deep weathering in the Shale Hills Critical Zone Observatory, Pennsylvania (USA): the hypothesis of nested chemical reaction fronts in the subsurface. *Earth Surf. Proc. Land.* **38**, 1280–1298.

Brantley S. L. and White A. F. (2009) Approaches to modeling weathered regolith. In Thermodynamics and Kinetics of Water-Rock Interaction (eds. E. H. Oelkers and J. Schott), pp. 435–484.

Brantley S. L., Yoxtheimer D., Arjmand S., Grieve P., Vidic R., Pollak J., Llewellyn G. T., Abad J. and Simon C. (2014) Water resource impacts during unconventional shale gas development: the Pennsylvania experience. *Int. J. Coal Geol.* **126**, 140–156.

Brunet J.-P. L., Li L., Karpyn Z. T. and Huerta N. J. (2016) Fracture opening or self-sealing: critical residence time as a unifying parameter for cement–CO_2–brine interactions. *Int. J. Greenhouse Gas Control* **47**, 25–37.

Casey W. H., Westrich H. R. and Holdren G. R. (1991) Dissolution rates of plagioclase at PH = 2 and 3. *Am. Miner.* **76**, 211–217.

Chapman E. C., Capo R. C., Stewart B. W., Kirby C. S., Hammack R. W., Schroeder K. T. and Edenborn H. M. (2012) Geochemical and strontium isotope characterization of produced waters from Marcellus shale natural gas extraction. *Environ. Sci. Technol.* **46**, 3545–3553.

Chou L. and Wollast R. (1985a) Steady-state kinetics and dissolution mechanisms of albite. *Am. J. Sci.* **285**, 963–993.

Chou L. and Wollast R. (1985b) Study of the weathering of albite at room-temperature and pressure with a fluidized-bed reactor - reply. *Geochim. Cosmochim. Acta* **49**, 1659–1660.

Drever J. I. and Stillings L. L. (1997) The role of organic acids in mineral weathering. *Colloids Surfaces A – Physicochem. Eng. Aspects* **120**, 167–181.

Gu X., Cole D. R., Rother G., Mildner D. F. R. and Brantley S. L. (2015) Pores in Marcellus Shale: a neutron scattering and FIB-SEM study. *Energy Fuels* **29**, 1295–1308.

Gu X., Mildner D. F., Cole D. R., Rother G., Slingerland R. and Brantley S. L. (2016) Quantification of organic porosity and water accessibility in Marcellus Shale using neutron scattering. *Energy Fuels* **30**, 4438–4449.

Gupta H. V., Sorooshian S. and Yapo P. O. (1998) Toward improved calibration of hydrologic models: multiple and noncommensurable measures of information. *Water Resour. Res.* **34**, 751–763.

Hasenmueller E. A., Jin L., Stinchcomb G. E., Lin H., Brantley S. L. and Kaye J. P. (2015) Topographic controls on the depth distribution of soil CO_2 in a small temperate watershed. *Appl. Geochem.* **63**, 58–69.

Hausrath E. M., Navarre-Sitchler A. K., Sak P. B., Steefel C. I. and Brantley S. L. (2008) Basalt weathering rates on Earth and the duration of liquid water on the plains of Gusev Crater, Mars. *Geology* **36**, 67–70.

House W. A. and Orr D. R. (1992) Investigation of the PH-dependence of the kinetics of quartz dissolution at 25 °C. *J. Chem. Soc.-Faraday Trans.* **88**, 233–241.

Huntington T. G. (2000) The potential for calcium depletion in forest ecosystems of southeastern United States: review and analysis. *Global Biogeochem. Cycles* **14**, 623–638.

Jaffe L. A., Peucker-Ehrenbrink B. and Petsch S. T. (2002) Mobility of rhenium, platinum group elements and organic carbon during black shale weathering. *Earth Planet. Sci. Lett.* **198**, 339–353.

Jin L., Andrews D. M., Holmes G. H., Lin H. and Brantley S. L. (2011) Opening the "Black Box": water chemistry reveals hydrological controls on weathering in the Susquehanna Shale Hills critical zone observatory. *Vadose Zone J.* **10**, 928–942.

Jin L., Ravella R., Ketchum B., Bierman P. R., Heaney P., White T. and Brantley S. L. (2010) Mineral weathering and elemental transport during hillslope evolution at the Susquehanna/Shale Hills Critical Zone Observatory. *Geochim. Cosmochim. Acta* **74**, 3669–3691.

Jin L. X., Mathur R., Rother G., Cole D., Bazilevskaya E., Williams J., Carone A. and Brantley S. (2013) Evolution of porosity and geochemistry in Marcellus formation black shale during weathering. *Chem. Geol.* **356**, 50–63.

Jin L. X., Ogrinc N., Yesavage T., Hasenmueller E. A., Ma L., Sullivan P. L., Kaye J., Duffy C. and Brantley S. L. (2014) The CO_2 consumption potential during gray shale weathering: insights from the evolution of carbon isotopes in the Susquehanna Shale Hills critical zone observatory. *Geochim. Cosmochim. Acta* **142**, 260–280.

Kalinowski B. E. and Schweda P. (2007) Rates and nonstoichiometry of vermiculite dissolution at 22 °C. *Geoderma* **142**, 197–209.

Kamei G. and Ohmoto H. (2000) The kinetics of reactions between pyrite and O-2-bearing water revealed from in situ monitoring of DO, Eh and pH in a closed system. *Geochim. Cosmochim. Acta* **64**, 2585–2601.

Kohler S. J., Dufaud F. and Oelkers E. H. (2003) An experimental study of illite dissolution kinetics as a function of pH from 1.4 to 12.4 and temperature from 5 to 50 °C. *Geochim. Cosmochim. Acta* **67**, 3583–3594.

Kolowith L. C. and Berner R. A. (2002) Weathering of phosphorus in black shales. Glob. Biogeochem. Cycles 16.

Kuechler R. and Noack K. (2007) Comparison of the solution behaviour of a pyrite-calcite mixture in batch and unsaturated sand column. *J. Contam. Hydrol.* **90**, 203–220.

Landrot G., Ajo-Franklin J. B., Yang L., Cabrini S. and Steefel C. I. (2012) Measurement of accessible reactive surface area in a sandstone, with application to CO_2 mineralization. *Chem. Geol.* **318**, 113–125.

Lasaga A. C. (1998) *Kinetic Theory in the Earth Sciences*. Princeton University Press, Princeton.

Lawrence C., Harden J. and Maher K. (2014) Modeling the influence of organic acids on soil weathering. *Geochim. Cosmochim. Acta* **139**, 487–507.

Lebedeva M. I., Fletcher R. C., Balashov V. N. and Brantley S. L. (2007) A reactive diffusion model describing transformation of bedrock to saprolite. *Chem. Geol.* **244**, 624–645.

Lebedeva M. I., Fletcher R. C. and Brantley S. L. (2010) A mathematical model for steady-state regolith production at constant erosion rate. *Earth Surf. Proc. Land.* **35**, 508–524.

Li L., Bao C., Sullivan P. L., Brantley S., Shi Y. and Duffy C. (2017a) Understanding watershed hydrogeochemistry: 2. Synchronized hydrological and geochemical processes drive stream chemostatic behavior. *Water Resour. Res.* **53**, 2346–2367.

Li L., Maher K., Navarre-Sitchler A., Druhan J., Meile C., Lawrence C., Moore J., Perdrial J., Sullivan P., Thompson A., Jin L., Bolton E. W., Brantley S. L., Dietrich W. E., Mayer K. U., Steefel C. I., Valocchi A., Zachara J., Kocar B., McIntosh J., Tutolo B. M., Kumar M., Sonnenthal E., Bao C. and Beisman J. (2017b) Expanding the role of reactive transport models in critical zone processes. *Earth Sci. Rev.* **165**, 280–301.

Li L., Salehikhoo F., Brantley S. L. and Heidari P. (2014) Spatial zonation limits magnesite dissolution in porous media. *Geochim. Cosmochim. Acta* **126**, 555–573.

Li L., Steefel C., Kowalsky M., Englert A. and Hubbard S. (2010) Effects of physical and geochemical heterogeneities on mineral transformation and biomass accumulation during a biostimulation experiment at Rifle, Colorado. *J. Contamin. Hydrol.* **112**, 45–63.

Lichtner P. C. (1992) Time-space continuum description of fluid rock interaction in permeable media. *Water Resour. Res.* **28**, 3135–3155.

Liermann L. J., Mathur R., Wasylenki L. E., Nuester J., Anbar A. D. and Brantley S. L. (2011) Extent and isotopic composition of Fe and Mo release from two Pennsylvania shales in the presence of organic ligands and bacteria. *Chem. Geol.* **281**, 167–180.

Liu R., Wolfe A. L., Dzombak D. A., Stewart B. W. and Capo R. C. (2008) Comparison of dissolution under oxic acid drainage conditions for eight sedimentary and hydrothermal pyrite samples. *Environ. Geol.* **56**, 171–182.

Luttge A., Arvidson R. S. and Fischer C. (2013) A stochastic treatment of crystal dissolution kinetics. *Elements* **9**, 183–188.

Malmstrom M., Banwart S., Lewenhagen J., Duro L. and Bruno J. (1996) The dissolution of biotite and chlorite at 25 °C in the near-neutral pH region. *J. Contam. Hydrol.* **21**, 201–213.

Mareschal L., Ranger J. and Turpault M. P. (2009) Stoichiometry of a dissolution reaction of a trioctahedral vermiculite at pH 2.7. *Geochim. Cosmochim. Acta* **73**, 307–319.

Mathur R., Jin L., Prush V., Paul J., Ebersole C., Fornadel A., Williams J. Z. and Brantley S. (2012) Cu isotopes and concentrations during weathering of black shale of the Marcellus Formation, Huntingdon County, Pennsylvania (USA). *Chem. Geol.* **304**, 175–184.

Millot R., Gaillardet J., Dupre B. and Allegre C. J. (2002) The global control of silicate weathering rates and the coupling with physical erosion: new insights from rivers of the Canadian Shield. *Earth Planet. Sci. Lett.* **196**, 83–98.

Molins S., Trebotich D., Miller G. H. and Steefel C.I. (2017) Mineralogical and transport controls on the evolution of porous media texture using direct numerical simulation. Water Resour. Res.

Molins S., Trebotich D., Steefel C.I. and Shen C. (2012) An investigation of the effect of pore scale flow on average geochemical reaction rates using direct numerical simulation. Water Resour. Res., 48.

Moore J. (2008) Biogeochemistry of Granitic Weathering. PhD Dissertation, pp. 26–28.

Moore J., Lichtner P. C., White A. F. and Brantley S. L. (2012) Using a reactive transport model to elucidate differences between laboratory and field dissolution rates in regolith. *Geochim. Cosmochim. Acta* **93**, 235–261.

Navarre-Sitchler A. and Brantley S. (2007) Basalt weathering across scales. *Earth Planet. Sci. Lett.* **261**, 321–334.

Navarre-Sitchler A., Steefel C. I., Yang L., Tomutsa L. and Brantley S. L. (2009) Evolution of porosity and diffusivity associated with chemical weathering of a basalt clast. J. Geophys. Res.-Earth Surface, 114.

Navarre-Sitchler A., Steefel C. I., Sak P. B. and Brantley S. L. (2011) A reactive-transport model for weathering rind formation on basalt. *Geochim. Cosmochim. Acta* **75**, 7644–7667.

Navarre-Sitchler A. K., Cole D. R., Rother G., Jin L., Buss H. L. and Brantley S. L. (2013) Porosity and surface area evolution during weathering of two igneous rocks. *Geochim. Cosmochim. Acta* **109**, 400–413.

Neaman A., Chorover J. and Brantley S. L. (2005) Implications of the evolution of organic acid moieties for basalt weathering over geological time. *Am. J. Sci.* **305**, 147–185.

Nugent M. A., Brantley S. L., Pantano C. G. and Maurice P. A. (1998) The influence of natural mineral coatings on feldspar weathering. *Nature* **395**, 588–591.

Obermajer M., Fowler M. G., Goodarzi F. and Snowdon L. R. (1997) Organic petrology and organic geochemistry of Devonian black shales in southwestern Ontario, Canada. *Org. Geochem.* **26**, 229–246.

Oelkers E. H., Schott J. and Devidal J. L. (1994) The effect of aluminum, pH, and chemical affinity on the rates of aluminosilicate dissolution reactions. *Geochim. Cosmochim. Acta* **58**, 2011–2024.

Peters C. A. (2009) Accessibilities of reactive minerals in consolidated sedimentary rock: an imaging study of three sandstones. *Chem. Geol.* **265**, 198–208.

Peucker-Ehrenbrink B. and Hannigan R. E. (2000) Effects of black shale weathering on the mobility of rhenium and platinum group elements. *Geology* **28**, 475–478.

Phan T. T., Capo R. C., Stewart B. W., Graney J. R., Johnson J. D., Sharma S. and Toro J. (2015) Trace metal distribution and mobility in drill cuttings and produced waters from Marcellus Shale gas extraction: uranium, arsenic, barium. *Appl. Geochem.* **60**, 89–103.

Poppe L. J., Paskevich V. F., Hathaway J. C., and Blackwood D. S. (2002) A laboratory manual for X-ray powder diffraction. U.S. Geological Survey Open File Report 01–041. U.S. Geological Survey, MA.

Reeves D. and Rothman D. H. (2013) Age dependence of mineral dissolution and precipitation rates. *Global Biogeochem. Cycles* **27**, 906–919.

Riebe C. S., Kirchner J. W. and Finkel R. C. (2004) Erosional and climatic effects on long-term chemical weathering rates in granitic landscapes spanning diverse climate regimes. *Earth Planet. Sci. Lett.* **224**, 547–562.

Salehikhoo F. and Li L. (2015) The role of magnesite spatial distribution patterns in determining dissolution rates: when do they matter? *Geochim. Cosmochim. Acta* **155**, 107–121.

Salehikhoo F., Li L. and Brantley S. L. (2013) Magnesite dissolution rates at different spatial scales: the role of mineral spatial distribution and flow velocity. *Geochim. Cosmochim. Acta* **108**, 91–106.

Steefel C. I., Appelo C. A. J., Arora B., Jacques D., Kalbacher T., Kolditz O., Lagneau V., Lichtner P. C., Mayer K. U., Meeussen J. C. L., Molins S., Moulton D., Shao H., Šimůnek J., Spycher N., Yabusaki S. B. and Yeh G. T. (2015) Reactive transport codes for subsurface environmental simulation. *Comput. Geosci.* **19**, 445–478.

Steefel C. I., DePaolo D. J. and Lichtner P. C. (2005) Reactive transport modeling: an essential tool and a new research approach for the Earth Sciences. *Earth Planet. Sci. Lett.* **240**, 539–558.

Stewart B. W., Chapman E. C., Capo R. C., Johnson J. D., Graney J. R., Kirby C. S. and Schroeder K. T. (2015) Origin of brines, salts and carbonate from shales of the Marcellus Formation: evidence from geochemical and Sr isotope study of sequentially extracted fluids. *Appl. Geochem.* **60**, 78–88.

Stillings L. L. and Brantley S. L. (1995) Feldspar dissolution at 25 °C and pH 3- reaction stoichiometry and the effect of cations. *Geochim. Cosmochim. Acta* **59**, 1483–1496.

Strang G. (1968) On the construction and comparison of difference schemes. *SIAM J. Numer. Anal.* **5**, 506–517.

Suchet P. A., Probst J. L. and Ludwig W. (2003) Worldwide distribution of continental rock lithology: implications for the atmospheric/soil CO_2 uptake by continental weathering and alkalinity river transport to the oceans. Glob. Biogeochem. Cycles, 17.

Suzuki-Muresan T., Vandenborre J., Abdelouas A. and Grambow B. (2011) Solution controls for dissolved silica at 25, 50 and 90 °C for quartz, Callovo-Oxfordian claystone, illite and MX80 bentonite. *Phys. Chem. Earth* **36**, 1648–1660.

Swoboda-colberg N. G. and Drever J. I. (1993) Mineral dissolution rates in plot-scale field and laboratory experiments. *Chem. Geol.* **105**, 51–69.

Truche L., Berger G., Destrigneville C., Guillaume D. and Giffaut E. (2010) Kinetics of pyrite to pyrrhotite reduction by hydrogen in calcite buffered solutions between 90 and 180 °C: implications for nuclear waste disposal. *Geochim. Cosmochim. Acta* **74**, 2894–2914.

Tuttle M. L. W. and Breit G. N. (2009) Weathering of the New Albany Shale, Kentucky, USA: I. Weathering zones defined by mineralogy and major-element composition. *Appl. Geochem.* **24**, 1549–1564.

Tuttle M. L. W., Breit G. N. and Goldhaber M. B. (2009) Weathering of the New Albany Shale, Kentucky: II. Redistribution of minor and trace elements. *Appl. Geochem.* **24**, 1565–1578.

Vidic R. D., Brantley S. L., Vandenbossche J. M., Yoxtheimer D. and Abad J. D. (2013) Impact of shale gas development on regional water quality. *Science* **340**, 9.

Warner N. R., Christie C. A., Jackson R. B. and Vengosh A. (2013) Impacts of shale gas wastewater disposal on water quality in western Pennsylvania. *Environ. Sci. Technol.* **47**, 11849–11857.

Wen H. and Li L. (2017) An upscaled rate law for magnesite dissolution in heterogeneous porous media. *Geochim. Cosmochim. Acta* **210**, 289–305.

Wen H., Li L., Crandall D. and Hakala J. A. (2016) Where lower calcite abundance creates more alteration: enhanced rock matrix diffusivity induced by preferential carbonate dissolution. Energy Fuels.

West A. J., Galy A. and Bickle M. (2005) Tectonic and climatic controls on silicate weathering. *Earth Planet. Sci. Lett.* **235**, 211–228.

White A. F. (1995) Chemical weathering rates of silicate minerals in soils. In *Chemical weathering rates of silicate minerals* (eds. A. F. White and S. L. Brantley). Mineralogical Society of America, Washington, D.C., pp. 407–461.

White A. F. and Brantley S. L. (2003) The effect of time on the weathering of silicate minerals: why do weathering rates differ in the laboratory and field? *Chem. Geol.* **202**, 479–506.

Whittemore D. O. and Langmuir D. (1974) Ferric oxyhydroxide microparticles in water. *Environ. Health Perspect.* **9**, 173.

Wildman R. A., Berner R. A., Petsch S. T., Bolton E. W., Eckert J. O., Mok U. and Evans J. B. (2004) The weathering of sedimentary organic matter as a control on atmospheric O_2: I. Analysis of a black shale. *Am. J. Sci.* **304**, 234–249.

Williamson M. A. and Rimstidt J. D. (1994) The kinetics and electrochemical rate-determining step of aqueous pyrite oxidation. *Geochim. Cosmochim. Acta* **58**, 5443–5454.

Yoshida T., Hayashi K. and Ohmoto H. (2002) Dissolution of iron hydroxides by marine bacterial siderophore. *Chem. Geol.* **184**, 1–9.

Zachara J., Brantley S., Chorover J., Ewing R., Kerisit S., Liu C., Perfect E., Rother G. and Stack A. (2016) Internal domains of natural porous media revealed: critical locations for transport, storage, and chemical reaction. *Environ. Sci. Technol.* **50**(6), 2811–2829.

Zheng L. G., Apps J. A., Zhang Y. Q., Xu T. F. and Birkholzer J. T. (2009) On mobilization of lead and arsenic in groundwater in response to CO_2 leakage from deep geological storage. *Chem. Geol.* **268**, 281–297.

Zysset A., Stauffer F. and Dracos T. (1994) Modeling of chemically reactive groundwater transport. *Water Resour. Res.* **30**, 2217–2228.

Associate editor: Brian W. Stewart